

## Euclid Quick Data Release (Q1)

### Extending the quest for little red dots to $z < 4$

Euclid Collaboration: L. Bisigello<sup>\*1</sup>, G. Rodighiero<sup>2,1</sup>, S. Fotopoulou<sup>3</sup>, F. Ricci<sup>4,5</sup>, K. Jahnke<sup>6</sup>, A. Feltre<sup>7</sup>, V. Allevalo<sup>8</sup>, F. Shankar<sup>9</sup>, P. Cassata<sup>2,1</sup>, E. Dalla Bontà<sup>2,1,10</sup>, G. Gandolfi<sup>11,1</sup>, G. Girardi<sup>2,1</sup>, M. Giuliatti<sup>12</sup>, A. Grazian<sup>1</sup>, C. C. Lovell<sup>13</sup>, R. Maiolino<sup>14</sup>, T. Matamoros Zatarain<sup>3</sup>, M. Mezcua<sup>15,16</sup>, I. Prandoni<sup>12</sup>, D. Roberts<sup>9</sup>, W. Roster<sup>17</sup>, M. Salvato<sup>17</sup>, M. Siudek<sup>18,15</sup>, F. Tarsitano<sup>19</sup>, Y. Toba<sup>20,21,22</sup>, A. Vietri<sup>2</sup>, L. Wang<sup>23,24</sup>, G. Zamorani<sup>25</sup>, M. Baes<sup>26</sup>, S. Belladitta<sup>6,25</sup>, A. Nersesian<sup>27,26</sup>, L. Spinoglio<sup>28</sup>, X. Lopez Lopez<sup>29,25</sup>, N. Aghanim<sup>30</sup>, B. Altieri<sup>31</sup>, A. Amara<sup>32</sup>, S. Andreon<sup>33</sup>, N. Auricchio<sup>25</sup>, H. Aussel<sup>34</sup>, C. Baccigalupi<sup>35,36,37,38</sup>, M. Baldi<sup>39,25,40</sup>, A. Balestra<sup>1</sup>, S. Bardelli<sup>25</sup>, A. Basset<sup>41</sup>, P. Battaglia<sup>25</sup>, R. Bender<sup>17,42</sup>, A. Biviano<sup>36,35</sup>, A. Bonchi<sup>43</sup>, E. Branchini<sup>44,45,33</sup>, M. Brescia<sup>46,8</sup>, J. Brinchmann<sup>47,48</sup>, S. Camera<sup>49,50,51</sup>, G. Cañas-Herrera<sup>52,53,54</sup>, V. Capobianco<sup>51</sup>, C. Carbone<sup>55</sup>, J. Carretero<sup>56,57</sup>, S. Casas<sup>58</sup>, M. Castellano<sup>5</sup>, G. Castignani<sup>25</sup>, S. Cavuoti<sup>8,59</sup>, K. C. Chambers<sup>60</sup>, A. Cimatti<sup>61</sup>, C. Colodro-Conde<sup>62</sup>, G. Congedo<sup>63</sup>, C. J. Conselice<sup>64</sup>, L. Conversi<sup>65,31</sup>, Y. Copin<sup>66</sup>, F. Courbin<sup>67,68</sup>, H. M. Courtois<sup>69</sup>, M. Cropper<sup>70</sup>, A. Da Silva<sup>71,72</sup>, H. Degaudenzi<sup>19</sup>, G. De Lucia<sup>36</sup>, A. M. Di Giorgio<sup>28</sup>, C. Dolding<sup>70</sup>, H. Dole<sup>30</sup>, F. Dubath<sup>19</sup>, C. A. J. Duncan<sup>64</sup>, X. Dupac<sup>31</sup>, S. Dusini<sup>73</sup>, A. Ealet<sup>66</sup>, S. Escoffier<sup>74</sup>, M. Farina<sup>28</sup>, R. Farinelli<sup>25</sup>, F. Faustini<sup>43,5</sup>, S. Ferriol<sup>66</sup>, F. Finelli<sup>25,75</sup>, M. Frailis<sup>36</sup>, E. Franceschi<sup>25</sup>, S. Galeotta<sup>36</sup>, K. George<sup>42</sup>, W. Gillard<sup>74</sup>, B. Gillis<sup>63</sup>, C. Giocoli<sup>25,40</sup>, P. Gómez-Alvarez<sup>76,31</sup>, J. Gracia-Carpio<sup>17</sup>, B. R. Granett<sup>33</sup>, F. Grupp<sup>17,42</sup>, S. Gwyn<sup>77</sup>, S. V. H. Haugan<sup>78</sup>, H. Hoekstra<sup>54</sup>, W. Holmes<sup>79</sup>, I. M. Hook<sup>80</sup>, F. Hormuth<sup>81</sup>, A. Hornstrup<sup>82,83</sup>, P. Hudelot<sup>84</sup>, M. Jhabvala<sup>85</sup>, E. Keihänen<sup>86</sup>, S. Kermiche<sup>74</sup>, A. Kiessling<sup>79</sup>, B. Kubik<sup>66</sup>, M. Kümmel<sup>42</sup>, M. Kunz<sup>87</sup>, H. Kurki-Suonio<sup>88,89</sup>, Q. Le Boulc'h<sup>90</sup>, A. M. C. Le Brun<sup>91</sup>, D. Le Mignant<sup>92</sup>, P. Liebing<sup>70</sup>, S. Ligorì<sup>51</sup>, P. B. Lilje<sup>78</sup>, V. Lindholm<sup>88,89</sup>, I. Lloro<sup>93</sup>, G. Mainetti<sup>90</sup>, D. Maino<sup>94,55,95</sup>, E. Maiorano<sup>25</sup>, O. Mansutti<sup>36</sup>, S. Marcin<sup>96</sup>, O. Marggraf<sup>97</sup>, M. Martinelli<sup>5,98</sup>, N. Martinet<sup>92</sup>, F. Marulli<sup>29,25,40</sup>, R. Massey<sup>99</sup>, S. Maurogordato<sup>100</sup>, E. Medinaceli<sup>25</sup>, S. Mei<sup>101,102</sup>, M. Melchior<sup>103</sup>, Y. Mellier<sup>104,84</sup>, M. Meneghetti<sup>25,40</sup>, E. Merlin<sup>5</sup>, G. Meylan<sup>105</sup>, A. Mora<sup>106</sup>, M. Moresco<sup>29,25</sup>, L. Moscardini<sup>29,25,40</sup>, R. Nakajima<sup>97</sup>, C. Neissner<sup>107,57</sup>, S.-M. Niemi<sup>52</sup>, J. W. Nightingale<sup>108</sup>, C. Padilla<sup>107</sup>, S. Paltani<sup>19</sup>, F. Pasian<sup>36</sup>, K. Pedersen<sup>109</sup>, W. J. Percival<sup>110,111,112</sup>, V. Pettorino<sup>52</sup>, S. Pires<sup>34</sup>, G. Polenta<sup>43</sup>, M. Poncet<sup>41</sup>, L. A. Popa<sup>113</sup>, L. Pozzetti<sup>25</sup>, F. Raison<sup>17</sup>, R. Rebolo<sup>114,115,62</sup>, A. Renzi<sup>2,73</sup>, J. Rhodes<sup>79</sup>, G. Riccio<sup>8</sup>, E. Romelli<sup>36</sup>, M. Roncarelli<sup>25</sup>, E. Rossetti<sup>39</sup>, H. J. A. Rottgering<sup>54</sup>, B. Rusholme<sup>116</sup>, R. Saglia<sup>42,17</sup>, Z. Sakr<sup>117,118,119</sup>, D. Sapone<sup>120</sup>, B. Sartoris<sup>42,36</sup>, J. A. Schewtschenko<sup>63</sup>, M. Schirmer<sup>6</sup>, P. Schneider<sup>97</sup>, T. Schrabback<sup>121</sup>, M. Scodreggio<sup>55</sup>, A. Secroun<sup>74</sup>, G. Seidel<sup>16,122,15</sup>, S. Serrano<sup>16,122,15</sup>, P. Simon<sup>97</sup>, C. Sirignano<sup>2,73</sup>, G. Sirri<sup>40</sup>, L. Stanco<sup>73</sup>, J. Steinwagner<sup>17</sup>, P. Tallada-Crespí<sup>56,57</sup>, A. N. Taylor<sup>63</sup>, H. I. Teplitz<sup>123</sup>, I. Tereno<sup>71,124</sup>, S. Toft<sup>125,126</sup>, R. Toledo-Moreo<sup>127</sup>, F. Torradeflot<sup>57,56</sup>, I. Tutusaus<sup>118</sup>, L. Valenziano<sup>25,75</sup>, J. Valiviita<sup>88,89</sup>, T. Vassallo<sup>42,36</sup>, G. Verdoes Kleijn<sup>24</sup>, A. Veropalumbo<sup>33,45,44</sup>, Y. Wang<sup>123</sup>, J. Weller<sup>42,17</sup>, A. Zacchei<sup>36,35</sup>, F. M. Zerbi<sup>33</sup>, I. A. Zinchenko<sup>42</sup>, E. Zucca<sup>25</sup>, M. Ballardini<sup>128,129,25</sup>, M. Bolzonella<sup>25</sup>, E. Bozzo<sup>19</sup>, C. Burigana<sup>12,75</sup>, R. Cabanac<sup>118</sup>, A. Cappi<sup>25,100</sup>, D. Di Ferdinando<sup>40</sup>, J. A. Escartin Vigo<sup>17</sup>, L. Gabarra<sup>130</sup>, M. Huertas-Company<sup>62,18,131,132</sup>, J. Martín-Fleitas<sup>106</sup>, S. Matthew<sup>63</sup>, M. Maturi<sup>117,133</sup>, N. Mauri<sup>61,40</sup>, A. Pezzotta<sup>17</sup>, M. Pöntinen<sup>88</sup>, C. Porciani<sup>97</sup>, I. Risso<sup>134</sup>, V. Scottez<sup>104,135</sup>, M. Sereno<sup>25,40</sup>, M. Tenti<sup>40</sup>, M. Viel<sup>35,36,38,37,136</sup>, M. Wiesmann<sup>78</sup>, Y. Akrami<sup>137,138</sup>, I. T. Andika<sup>139,140</sup>, S. Anselmi<sup>73,2,141</sup>, M. Archidiacono<sup>94,95</sup>, F. Atrio-Barandela<sup>142</sup>, C. Benoist<sup>100</sup>, K. Benson<sup>70</sup>, D. Bertacca<sup>2,1,73</sup>, M. Bethermin<sup>143</sup>, A. Blanchard<sup>118</sup>, L. Blot<sup>144,141</sup>, M. L. Brown<sup>64</sup>, S. Bruton<sup>145</sup>, A. Calabro<sup>5</sup>, F. Caro<sup>5</sup>, C. S. Carvalho<sup>124</sup>, T. Castro<sup>36,37,35,136</sup>, Y. Charles<sup>92</sup>, F. Cogato<sup>29,25</sup>, T. Contini<sup>118</sup>, A. R. Cooray<sup>146</sup>, O. Cucciati<sup>25</sup>, S. Davini<sup>45</sup>, F. De Paolis<sup>147,148,149</sup>, G. Desprez<sup>24</sup>, A. Díaz-Sánchez<sup>150</sup>, J. J. Diaz<sup>62</sup>, S. Di Domizio<sup>44,45</sup>, J. M. Diego<sup>151</sup>, A. Enia<sup>39,25</sup>, Y. Fang<sup>42</sup>, A. G. Ferrari<sup>40</sup>, P. G. Ferreira<sup>130</sup>, A. Finoguenov<sup>88</sup>, A. Fontana<sup>5</sup>, F. Fontanot<sup>36,35</sup>, A. Franco<sup>148,147,149</sup>, K. Ganga<sup>101</sup>, J. García-Bellido<sup>137</sup>, T. Gasparotto<sup>36</sup>, V. Gautard<sup>152</sup>, E. Gaztanaga<sup>15,16,13</sup>, F. Giacomini<sup>40</sup>, F. Gianotti<sup>25</sup>, G. Gozaliasl<sup>153,88</sup>, M. Guidi<sup>39,25</sup>, C. M. Gutierrez<sup>154</sup>, A. Hall<sup>63</sup>, W. G. Hartley<sup>19</sup>, S. Hemmati<sup>116</sup>, C. Hernández-Monteagudo<sup>115,62</sup>, H. Hildebrandt<sup>155</sup>, J. Hjorth<sup>109</sup>, J. J. E. Kajava<sup>156,157</sup>, Y. Kang<sup>19</sup>, V. Kansal<sup>158,159</sup>, D. Karagiannis<sup>128,160</sup>, K. Kiiveri<sup>86</sup>, C. C. Kirkpatrick<sup>86</sup>, S. Kruk<sup>31</sup>, J. Le Graet<sup>74</sup>, L. Legrand<sup>161,162</sup>, M. Lembo<sup>128,129</sup>, F. Lepori<sup>163</sup>, G. Leroy<sup>164,99</sup>, G. F. Lesci<sup>29,25</sup>, J. Lesgourgues<sup>58</sup>, L. Leuzzi<sup>29,25</sup>, T. I. Liaudat<sup>165</sup>, A. Loureiro<sup>166,167</sup>, J. Macias-Perez<sup>168</sup>, G. Maggio<sup>36</sup>, M. Magliocchetti<sup>28</sup>, E. A. Magnier<sup>60</sup>, C. Mancini<sup>55</sup>, F. Mannucci<sup>7</sup>, R. Maoli<sup>169,5</sup>, C. J. A. P. Martins<sup>170,47</sup>, L. Maurin<sup>30</sup>, M. Miluzio<sup>31,171</sup>, P. Monaco<sup>172,36,37,35</sup>, C. Moretti<sup>38,136,36,35,37</sup>, G. Morgante<sup>25</sup>, S. Nadathur<sup>13</sup>, K. Naidoo<sup>13</sup>, A. Navarro-Alsina<sup>97</sup>,

S. Nesseris<sup>137</sup>, F. Passalacqua<sup>2, 73</sup>, K. Paterson<sup>6</sup>, L. Patrizzi<sup>40</sup>, A. Pisani<sup>74, 173</sup>, D. Potter<sup>163</sup>, S. Quai<sup>29, 25</sup>, M. Radovich<sup>1</sup>, P.-F. Rocci<sup>30</sup>, S. Sacquegna<sup>147, 148, 149</sup>, M. Sahlén<sup>174</sup>, D. B. Sanders<sup>60</sup>, E. Sarpa<sup>38, 136, 37</sup>, C. Scarlata<sup>175</sup>, J. Schaye<sup>54</sup>, A. Schneider<sup>163</sup>, D. Sciotti<sup>5, 98</sup>, E. Sellentin<sup>176, 54</sup>, A. Shulevski<sup>177, 24, 54, 178</sup>, L. C. Smith<sup>179</sup>, K. Tanidis<sup>130</sup>, C. Tao<sup>74</sup>, G. Testera<sup>45</sup>, R. Teyssier<sup>173</sup>, S. Tosi<sup>44, 134</sup>, A. Troja<sup>2, 73</sup>, M. Tucci<sup>19</sup>, C. Valieri<sup>40</sup>, A. Venhola<sup>180</sup>, D. Vergani<sup>25</sup>, G. Verza<sup>181</sup>, P. Vielzeuf<sup>74</sup>, A. Viitanen<sup>86, 5</sup>, N. A. Walton<sup>179</sup>, J. R. Weaver<sup>182</sup>, E. Soubrie<sup>30</sup>, and D. Scott<sup>183</sup>

(Affiliations can be found after the references)

Received 14 March 2025; Accepted 19 July 2025

## ABSTRACT

Recent observations with the *James Webb* Space Telescope (JWST) have revealed an interesting population of sources with a compact morphology and a characteristic v-shaped continuum, namely blue at a rest frame  $\lambda < 4000 \text{ \AA}$  and red at longer wavelengths. The nature of these sources, which are called little red dots (LRDs), is still highly debated because it is unclear whether they host active galactic nuclei (AGNs) and their number seems to drop drastically at  $z < 4$ . We took advantage of the  $63 \text{ deg}^2$  covered by the quick *Euclid* Quick Data Release (Q1) to extend the search for LRDs to brighter magnitudes and lower redshifts than what was possible with JWST. This is fundamental for a broader view of the evolution of this peculiar galaxy population. The selection was performed by fitting the available photometric data (*Euclid*, the *Spitzer* Infrared Array Camera (IRAC), and ground-based *griz* data) with two power laws to retrieve the rest-frame optical and UV slopes consistently over a wide redshift range (i.e.  $z < 7.6$ ). We then excluded extended objects and possible line emitters and inspected the data visually to remove any imaging artefacts. The final selection included 3341 LRD candidates from  $z = 0.33$  to  $z = 3.6$ , 29 of which were also detected in IRAC. The resulting rest-frame UV luminosity function, in contrast with previous JWST studies, shows that the number density of LRD candidates increases from high redshift to  $z = 1.5\text{--}2.5$  and decreases at even lower redshifts. The subsample of more robust LRD candidates that are also detected with IRAC show a weaker evolution, however, which is affected by low statistics and limited by the IRAC resolution. The comparison with previous quasar UV luminosity functions shows that LRDs are not the dominant AGN population at  $z < 4$  and  $M_{UV} < -21$ . Follow-up studies of these LRD candidates are pivotal to confirm their nature, probe their physical properties, and determine whether they are compatible with JWST sources because the different spatial resolution and wavelength coverage of *Euclid* and JWST might select different samples of compact sources.

**Key words.** Galaxies: active - Galaxies: luminosity function - Galaxies: evolution

## 1. Introduction

Supermassive black holes (SMBHs) with tens of millions of solar masses appear to be ubiquitous at the centres of local galaxies (e.g. Magorrian et al. 1998; Gültekin et al. 2009). Moreover, a close co-evolution that links SMBHs to their host galaxies is suggested by the tight scaling relations that are observed between the SMBH masses and different galactic properties (e.g. Magorrian et al. 1998; Silk & Rees 1998; Gebhardt et al. 2000; Ferrarese 2002; Mullaney et al. 2012; Delvecchio et al. 2022). Theoretical models calibrated against present-day scaling relations seem to produce a wide range of SMBH properties at higher redshifts, however, which arise from the differences in the implementation of supernova and BH feedback and sub-grid physics (e.g. Habouzit et al. 2020, 2021). It is therefore important to extend the analysis of SMBHs and their host galaxies to a wide range of times.

Observational evidence for massive accreting BHs that shine as active galactic nuclei (AGNs) at increasingly higher redshifts places strong constraints on their formation scenarios and the mass of their seeds. The formation of a  $10^9 M_\odot$  SMBH by  $z = 7$  requires a heavy seed ( $M_{\text{BH}} \sim 10^5 M_\odot$ ), a light seed ( $M_{\text{BH}} \sim 10^2 M_\odot$ ) that accretes for some time at super-Eddington or hyper-Eddington rates (e.g. Wyithe & Loeb 2012; Alexander & Natarajan 2014; Inayoshi et al. 2016; Begelman & Volonteri 2017; Pacucci et al. 2017; Pacucci & Loeb 2022; Maiolino et al. 2024c), or primordial BHs that formed as a result of fluctuations in the early Universe (Hawking 1971; Carr & Hawking 1974; Dayal et al. 2025). It is unclear, however, whether the currently observed high- $z$  AGNs can be considered representative of the whole AGN population. The study of low-luminosity AGNs and low-mass SMBHs is therefore key to placing constraints on the mass distribution for seeds of high- $z$  AGNs.

The epoch of reionisation marks the transition phase at which the first sources of ultraviolet (UV) radiation were able, after the so-called dark ages, to ionise hydrogen atoms in the surrounding intergalactic medium for the first time (Barkana & Loeb 2001; Dayal & Ferrara 2018). It is still largely debated which sources caused this process, however. Many studies identified low-mass metal-poor star-forming galaxies at high redshift as the main driver of cosmic reionisation (e.g. Atek et al. 2024; Simmonds et al. 2024; Dayal 2024), and others showed evidence that faint AGNs can contribute significantly to reionisation (e.g. Asthana et al. 2024) and in some cases dominate reionisation (e.g. Madau et al. 2024; Grazian et al. 2024). It is therefore fundamental to quantify the number density of these faint AGNs to constrain their contribution to the reionisation of the Universe.

The first years of observations with the *James Webb* Space Telescope (JWST) have revealed a new intriguing population of compact red sources that are characterised by a peculiar v-shaped spectral energy distribution (SED), namely a blue rest-frame UV continuum and a steep red slope in the rest-frame optical (e.g. Kocevski et al. 2023, 2024; Harikane et al. 2023; Matthee et al. 2024; Greene et al. 2024; Labbé et al. 2023; Labbé et al. 2023; Killi et al. 2024; Furtak et al. 2023). These so-called little red dots (LRDs) are mainly observed at  $z \geq 4$  and can easily be selected by photometric observations because their morphology is compact and their SED shape is peculiar. Particular care needs to be taken to remove contaminating populations, however, such as brown dwarfs, which correspond to 21% of the colour-selected JWST LRD candidates according to Langeroodi & Hjorth (2023).

The nature of these LRDs is heavily debated. Their steep rest-frame optical slopes are consistent with either a reddened AGN continuum or emission from dusty star formation (e.g. Kocevski et al. 2023; Barro et al. 2023; Labbé et al. 2023; Akins et al. 2024), with evidence supporting both scenarios. For exam-

\* e-mail: laura.bisigello@inaf.it

ple, spectroscopic follow-up studies of LRDs have shown that about 80% of them show broad hydrogen ( $H\alpha$  and  $H\beta$ ) emission (e.g. [Kocevski et al. 2023, 2024](#); [Kokorev et al. 2024a](#); [Killi et al. 2024](#); [Matthee et al. 2024](#); [Furtak et al. 2023](#); [Greene et al. 2024](#); [Wang et al. 2024](#)), with general line widths with an FWHM  $\leq 1000 \text{ km s}^{-1}$ , but some even reach  $3000 \text{ km s}^{-1}$ . These line widths would far exceed those of typical star-forming galaxies at lower redshift (e.g. [Fumagalli et al. 2012](#)), which supports the AGN scenario. In this picture, we have a direct view of the broad-line region and the accretion disk of the AGN, but with foreground dust attenuation that either originates from a dusty interstellar medium (ISM) or from nuclear dust (see, e.g. [Netzer 2015](#); [Hickox & Alexander 2018](#)). This scenario would mean that LRDs are similar to the red quasars that are observed at lower redshifts (e.g. [Webster et al. 1995](#); [Richards et al. 2003](#); [Urrutia et al. 2008](#); [Glikman et al. 2012, 2015](#)), considering also that some of these red quasar show a similar excess of UV light ([Wethers et al. 2018](#); [Stepney et al. 2024](#)). While the majority of LRDs may host an AGN, they represent a sub-sample of the overall AGN population. Out of the large number of broad-line AGNs discovered by JWST, only 10–30% have SEDs that are typical of LRDs ([Hainline et al. 2024](#)).

The SMBH masses inferred for these LRDs lie in the range  $M_{\text{BH}} = 10^6\text{--}10^8 M_{\odot}$ , and their stellar masses range from  $10^7$  to  $10^{11} M_{\odot}$ . This shows that a fraction of them are over-massive relative to the stellar masses of their host galaxies when compared to the local  $M_{\text{BH}}\text{--}M_*$  relation (e.g. [Maiolino et al. 2024b](#); [Harikane et al. 2023](#)), and they are consistent with the local relation between  $M_{\text{BH}}$  and stellar velocity dispersion ([Maiolino et al. 2024b](#)). This finding indicates they may be going through super-Eddington accretion or originate from heavy BH seeds. [Bellovary \(2025\)](#) instead recently hypothesised that LRDs might be runaway-collapse globular clusters with tidal disruption events, which might explain their compact size, UV luminosities, and high number densities.

In the scenario in which LRDs are entirely powered by dusty starbursts, they would correspond to very massive galaxies ( $M_* = 10^9\text{--}10^{11} M_{\odot}$ ). In this picture, a final excess of massive early galaxies would be reached, but some of which would contradict cosmological models and some would be so compact as to be unstable against supernovae feedback ([Wang et al. 2024](#); [Akins et al. 2024](#)). This supports the AGN scenario. Mid-infrared (mid-IR) observations at  $5\text{--}25 \mu\text{m}$  have shown a remarkably flat continuum, however, which favours SED models consistent with a dusty compact starburst and only a mild contribution from an obscured AGN ([Williams et al. 2024](#); [Pérez-González et al. 2024](#)) or an AGN torus without hot dust ([Leung et al. 2024](#); [Barro et al. 2024](#)). Only two LRDs have been detected in the far-IR so far, which provides some indications of warm dust emission ([Barro et al. 2024](#); [Juodžbalis et al. 2024](#)), and many other LRDs have not been detected in the far-IR. This limits the possible presence of cool or warm dust that is linked to star formation ([Labbe et al. 2025](#)). Moreover, the spectra of several broad-line objects show a clear Balmer break, which implies that evolved stars might indeed contribute to the rest-frame optical ([Kokorev et al. 2024b](#)). The precise contribution is highly degenerate, however ([Wang et al. 2024](#)).

In addition, the majority of LRDs are not strong X-ray emitters. They are undetected (or only marginally detected) even in very deep observations or in a stacking analysis ([Ananna et al. 2024](#); [Yue et al. 2024](#)). For this reason, some studies have hypothesised that the broad-line components cannot be due to an AGN, but to outflows driven by star formation or inelastic Raman scattering of stellar UV continua by neutral hydrogen atoms

([Kokubo & Harikane 2024](#)). Alternatively, other studies have reported that the broadening might be consistent with the stellar velocity dispersion if the galaxy were going through a short-lived phase when the central densities are much higher than at later times ([Baggen et al. 2024](#)). Other studies have instead suggested that the X-ray weakness might be due to a very steep X-ray spectrum that is induced by the absorption by large Compton-thick columns or a very high BH accretion rate ([Maiolino et al. 2024a](#)). The last two scenarios would also explain the non-detection at radio frequencies ([Mazzolari et al. 2024](#)). The dense neutral gas around the AGN accretion disk would also mimic a Balmer break, which indicates that the rest-frame optical may not be due to evolved stars ([Inayoshi & Maiolino 2024](#)). The absence of variability in the rest-frame UV, except for a few LRDs ([Zhang et al. 2024](#)), may argue against a strong contribution by AGN, however ([Tee et al. 2024](#); [Kokubo & Harikane 2024](#)).

The uncertainties on the nature of the LRDs are, at least partially, driven by their high- $z$  nature, which implies that they are faint and require near-IR observations. While preliminary studies trying to find low- $z$  and local analogues have been performed by, for example, [Noboriguchi et al. \(2023\)](#), [Mezcua et al. \(2024\)](#), and [Lin et al. \(2024\)](#), large near-IR surveys are necessary to follow the redshift evolution of LRDs because their number density has been suggested to dramatically drop at  $z < 4$  ([Kocevski et al. 2024](#)). Moreover, large near-IR surveys like this are key for probing the LRD clustering on large scales. [Tanaka et al. \(2024\)](#) already suggested that LRDs may show an excess of clustering at kiloparsec scales. The large observed area and the near-IR coverage of *Euclid* ([Euclid Collaboration: Mellier et al. 2025](#)) is therefore ideal to search for and study LRDs.

We searched for LRDs using the newly available [Euclid Quick Release Q1 \(2025\)](#), combined with publicly available images from the *Spitzer* Infrared Array Camera (IRAC) and ground-based optical data. The area and depth of these *Euclid* observations are ideal for a first characterisation of the bright end of the LRD luminosity function and to extend the search to  $z < 4$ . To select LRDs, we follow the approach by [Kocevski et al. \(2024\)](#) and select them using cuts on the rest-frame optical and UV slopes. The paper is structured as follows. In [Sect. 2](#) we present a summary of the *Euclid* data products we used, as well as the ancillary IRAC images. In [Sect. 3](#) we outline our selection method, and we discuss our findings in [Sect. 4](#). The final conclusion and future prospects are reported in [Sect. 5](#). Throughout the paper, we consider a  $\Lambda$ CDM cosmology with  $H_0 = 70 \text{ km s}^{-1} \text{ Mpc}^{-1}$ ,  $\Omega_m = 0.27$ , and  $\Omega_{\Lambda} = 0.73$ . All magnitudes are reported in the AB system ([Oke & Gunn 1983](#)).

## 2. Data description

### 2.1. *Euclid* data products

The Q1 data release was described by [Euclid Collaboration: Aussel et al. \(2025\)](#), the Visible Camera (VIS) and Near-Infrared Spectrometer and Photometer (NISF) processing and data products were reported by [Euclid Collaboration: McCracken et al. \(2025\)](#) and [Euclid Collaboration: Polenta et al. \(2025\)](#), respectively, and the photometric catalogue was discussed in [Euclid Collaboration: Romelli et al. \(2025\)](#). An overview of the scientific objectives of the *Euclid* ESA mission was reported in [Euclid Collaboration: Mellier et al. \(2025\)](#).

Briefly, Q1 includes  $63 \text{ deg}^2$  of the extragalactic sky, divided into three fields:  $22 \text{ deg}^2$  in the Euclid Deep Field North (EDF-N);  $12 \text{ deg}^2$  in the Euclid Deep Field Fornax (EDF-F); and  $28 \text{ deg}^2$  in the Euclid Deep Field South (EDF-S). Each field has

**Table 1.** Filters and associated observed depths.

Band	$\lambda_{\text{eff}}$ [ $\mu\text{m}$ ]	EDF-F	EDF-N	EDF-S
CFHT/MegaCam <i>u</i>	0.372		23.4	
HSC <i>g</i>	0.480		24.9	
CFHT/MegaCam <i>r</i>	0.640		24.0	
PAN-STARRS <i>i</i>	0.755		23.1	
HSC <i>z</i>	0.891		23.3	
Decam <i>g</i>	0.473	24.6		24.7
Decam <i>r</i>	0.642	24.3		24.4
Decam <i>i</i>	0.784	23.8		23.8
Decam <i>z</i>	0.926	23.1		23.1
VIS/ $I_E$	0.715	24.7	24.7	24.7
NISP/ $Y_E$	1.085	23.1	23.2	23.1
NISP/ $J_E$	1.375	23.2	23.3	23.3
NISP/ $H_E$	1.773	23.2	23.2	23.2
IRAC/IRAC1	3.550	24.0	24.0	23.1
IRAC/IRAC2	4.493	24.0	24.0	23.0
IRAC/IRAC3	5.696	21.2	20.0	
IRAC/IRAC4	7.799	19.9	21.1	

**Notes.** The reported magnitudes are the  $10\sigma$  observed depths. The optical and *Euclid* magnitudes refer to an extended source in an aperture with a diameter of  $2 \times \text{FWHM}$  and correspond to the median depths of the observing tiles (Euclid Collaboration: Romelli et al. 2025). For the IRAC1 and IRAC2 values, see Euclid Collaboration: Moneti et al. (2022) and Euclid Collaboration: McPartland et al. (2025). The depths correspond to average values in the fields that were derived considering empty apertures of  $2''$ . For the IRAC3 and IRAC channels, we report the average depths derived from the catalogue after correction of the aperture to the total magnitudes.

been observed in four photometric bands, one band in the visible ( $I_E$ , Euclid Collaboration: Cropper et al. 2025), and three bands in the near-IR (NISP,  $Y_E$ ,  $J_E$ , and  $H_E$  band, see Euclid Collaboration: Jahnke et al. 2025). In addition, these observations are complemented with ground-based observations that are carried out with multiple instruments and cover between  $0.3 \mu\text{m}$  and  $0.9 \mu\text{m}$ . They are part of the Ultraviolet Near-Infrared Optical Northern Survey (UNIONS; Gwyn et al. in prep.) or the Dark Energy Survey (Abbott et al. 2018). The complete list of available filters in each field and their corresponding observational depths are reported in Table 1.

We considered aperture photometry measured for all bands on the images convolved to the lowest spatial resolution (usually a ground-based band). We considered an aperture with a diameter of two full widths at half maximum (FWHM; a median value of  $1''.3$ ), and we corrected it to the total (see Euclid Collaboration: Romelli et al. 2025, for more details). We also corrected each flux for Galactic extinction using the position of each source and the relation by Gordon et al. (2023), which strongly relies on the results by Gordon et al. (2009); Fitzpatrick et al. (2019); Gordon et al. (2021), and Declair et al. (2022).

## 2.2. IRAC photometry

We started from the collection of IRAC images described by Euclid Collaboration: Moneti et al. (2022), which cover a fraction of the Euclid Deep Fields (EDFs) as part of the Cosmic Dawn survey (Euclid Collaboration: McPartland et al. 2025). The images result from a collection of different programmes with a non-uniform coverage in area and depth. We report the average  $10\sigma$  depths in Table 1 and the area coverage in Table 2. The IRAC3

**Table 2.** Area coverage in  $\text{deg}^2$  of the available IRAC images (Euclid Collaboration: Moneti et al. 2022).

Channel	EDF-F	EDF-N	EDF-S
IRAC1	10.52	11.74	23.60
IRAC2	11.05	11.54	23.14
IRAC3	7.78	0.61	...
IRAC4	7.77	0.62	...

and IRAC4 filters are only available for a small portion of the EDF-F and EDF-N, and none is available for the EDF-S.

Starting from the public images, we removed the sky background using the Python package PHOTUTILS (Bradley et al. 2023). We derived the median value using a filter with  $3 \text{ pixel} \times 3 \text{ pixels}$ . With the same package, we then used the position of all *Euclid* sources to extract aperture photometry with an aperture radius of  $1''$ , which is consistent with half the smallest FWHM of IRAC, from all available IRAC images. In this preliminary work, no attempt was made to de-blend IRAC sources using the *Euclid* positions. For this reason, we visually confirmed the selected LRD candidates to remove objects that were affected by blending.

To derive the correction for the aperture to the total fluxes for all four IRAC filters, we compared this catalogue with a separate extraction that was performed for the EDF-N alone (Bisigello et al. 2025). The extraction was performed using the co-added IRAC1 and IRAC2 images as the detection image, weighted for each uncertainty map, and considering Kron apertures that were derived with a scaling parameter of the unscaled Kron radius of 1.8 and a minimum value for the unscaled Kron radius of 2.5 pixels. We then matched the two EDF-N catalogues with the aperture and Kron fluxes to derive the aperture-to-total correction in each filter. We applied the same correction in all three fields.

We verified that the total fluxes were consistent with the catalogues described by Euclid Collaboration: Zalesky et al. (2025), which only cover two out of three EDFs, however, and only include the IRAC1 and IRAC2 filters. The comparison is shown in Appendix A. The magnitudes we derived are clearly brighter on average by 0.1 magnitudes in the EDF-F and by 0.3 magnitudes in the EDF-N than the magnitudes presented in the Cosmic Dawn Catalogue. The agreement is, however, within 0.1 magnitudes when we only consider bright objects (i.e. IRAC1 or IRAC2  $< 21$ ).

## 2.3. Photometric redshifts

As a first estimate of the photometric redshift, we considered the median value and the two first modes derived in the main *Euclid* pipeline, which were described in detail by Euclid Collaboration: Tucci et al. (2025). Because these estimates are limited to  $z = 6$ , we also considered the redshift estimate derived for NISP-detected objects. This extended the redshift range to  $z = 12$ . In this case, we considered the redshift of the highest peak of the probability distribution as the best estimate. As tested by Appendix B, the redshift estimation for LRDs derived from the pipeline includes about 40% of outliers because LRD templates are not included in the pipeline at the moment. We discuss the method we used to improve these estimates below.

## 3. Sample selection

Previous JWST photometric studies mainly identified LRDs by applying some colour cuts to compact sources (e.g. Barro et al.

**Table 3.** Number of sources retrieved in the different steps of the LRD selection in the three EDFs.

	EDF-F	EDF-N	EDF-S
Total sources	5 328 489	11 378 352	13 060 965
Reliable objects	3 640 908	7 342 804	8 588 063
IRAC-detected, $z \leq 6$	2 762 173	2 556 970	4 388 869
$N_{\text{filter}, S/N > 3} \geq 4$	1 094 377 (43%)	631 576 (23%)	1 850 820 (43%)
v-shaped continuum	891 (0.08%)	616 (0.09%)	3848 (0.2%)
Compact	42 (5%)	22 (4%)	173 (5%)
No emission lines	20 (48%)	8 (36%)	86 (50%)
$\chi^2 < 100$	16 (80%)	7 (87%)	82 (94%)
Visual inspection	8 (50%)	1 (14%)	20 (24%)
No-IRAC, $z \leq 2.1$	1 021 175	4 520 496	3 935 178
$N_{\text{filter}, S/N > 3} \geq 4$	189 275 (18%)	692 437 (15%)	735 675 (19%)
v-shaped continuum	15 838 (8%)	45 797 (7%)	59 035 (8%)
Compact	624 (4%)	1611 (3%)	2804 (5%)
No emission lines	558 (90%)	1344 (83%)	2560 (91%)
$\chi^2 < 100$	546 (87%)	1233 (76%)	2509 (98%)
Visual inspection	422 (77%)	970 (79%)	1920 (76%)
Total $z > 6$ candidates	24 050	71 776	53 131
Reliable galaxies	12 325 (51%)	27 535 (38%)	42 564 (80%)
IRAC-detected	3508 (28%)	5024 (18%)	4534 (11%)
$N_{\text{filter}, S/N > 3} \geq 4$	1883 (54%)	3098 (62%)	1617 (36%)
v-shaped continuum	103 (5%)	128 (4%)	68 (4%)
Compact	0	0	0

**Notes.** The different selections are described in Sect. 3. The percentages correspond to the percentage of objects that was selected in one line with respect to the line above.

2023; Labbe et al. 2023; Kokorev et al. 2024a). This type of selection is difficult to apply directly to *Euclid*, however, because the filter set is different. In addition, a simple colour cut does not allow us to select the sources uniformly at different redshifts because it is based on observed and not on rest-frame properties. Therefore, we considered the alternative approach adopted by Kocevski et al. (2024) and selected sources with a compact morphology, a red continuum in the rest-frame optical wavelengths, and a blue continuum in the the rest-frame UV. The latter two quantities were directly derived by fitting the available photometric data. We report the entire classification procedure we applied in detail below, and we report in Table 3 the original source number in each field and the change in this number at the different selection steps.

### 3.1. LRD selection procedure

As a first conservative selection, we removed objects that were classified as stars (PHZ\_CLASSIFICATION = 1) using the classification from the PHZ processing function (Euclid Collaboration: Tucci et al. 2025). This classification is based on photometry and not on compactness. This is fundamental to avoid removing any LRD candidates. We also retrieved only galaxies from the *Euclid* archive with reliable photometry, which we defined as having DET\_QUALITY\_FLAG = 0, SPURIOUS\_FLAG = 0, and FLAG = 0 for any *Euclid* filter. This selection allowed us to remove objects in the proximity of bright stars, blended sources, saturated or bad pixels, and sources that are contaminated by close neighbours. We refer to the subsample of objects that we obtained after this selection step as reliable objects.

We proceeded by removing objects outside the area that is covered by IRAC observations because these bands are fundamental to extending the search of LRDs at  $z > 2$ . For the same

reason, we only kept objects with a signal-to-noise ratio  $S/N > 3$  in the IRAC1 or IRAC2 filter. We refer to these objects as IRAC-detected sources. Moreover, to fit the UV and the optical rest-frame continuum simultaneously, we only considered objects with  $S/N > 3$  in more than four filters. We also ensured that at least two filters traced the rest-frame UV continuum and two filters traced the rest-frame optical continuum.

We continued by selecting only sources with the characteristic v-shaped continuum, following the approach by Kocevski et al. (2024), as described above. In particular, the continuum slope  $\beta$ , defined such that  $f_\lambda \propto \lambda^\beta$ , was determined by performing a  $\chi^2$  minimisation fit to the observed magnitudes,

$$m_i = -2.5 (\beta + 2) \log_{10} \left( \frac{\lambda_i}{\lambda_{\text{break}}} \right) + c, \quad (1)$$

where  $m_i$  is the AB magnitude measured in the  $i$ th filter with an effective wavelength of  $\lambda_i$ , and  $\lambda_{\text{break}} = 3645 \text{ \AA}$  is the wavelength of the break of the v-shape continuum. This fit was performed to derive the rest-frame UV and optical spectral slopes  $\beta_{\text{UV}}$  and  $\beta_{\text{opt}}$ . In Fig. 1 we report the filters we used to fit  $\beta_{\text{UV}}$  and  $\beta_{\text{opt}}$  at different redshifts considering the *Euclid*, ground-based bands and the IRAC1 and IRAC2 IRAC filters. We considered a filter to trace the rest-frame UV or optical part of the SED when the filter was totally redward or blueward  $\lambda_{\text{break}}$  to avoid the redshift interval in which the filter is at the break. Based on the filter availability and considering the small area coverage by the two longest IRAC filters, the fit was mainly possible between  $z = 1$  and  $z = 7.6$  for the EDF-F and EDF-S, but it can be extended to  $z = 0.6$  in the EDF-N based on the  $u$ -band observations. In the same plot, we report for comparison the redshift range in which at least two JWST NIRCcam broad-band filters cover the rest-frame UV and optical parts of the SED. The absence of the shortest filters, which are rarely included in JWST

surveys, would push the blue limit to higher redshifts. The NIR-Cam medium- or narrow-band filters or the MIRI bands might instead increase the redshift range in which the LRD analysis can be performed.

The LRD redshifts are not correctly recovered by the standard *Euclid* pipeline (see Appendix B) because LRD templates are currently not included. We therefore included the redshift as a free parameter in the fit. We considered the median redshift from the pipeline as an initial guess and the first- and second-mode redshifts (i.e. first and second peak in the redshift probability distribution) as limits. For candidates at  $z > 6$ , the photometric redshift was derived considering a secondary branch of the pipeline. In this case, we therefore considered the first peak of the redshift probability distribution as the initial guess. The fit was performed with the *Scipy* package (Virtanen et al. 2020). To take possible unknown uncertainties into account, we added 5% of the flux in quadrature to the flux uncertainties. In the fit, we considered all available filters, but we included fluxes with  $S/N < 3$  as 0 with an error equal to twice the flux uncertainties to take unknown uncertainties into account. The uncertainties on the output properties were derived by repeating the fit 100 times after randomising the fluxes, considering a Gaussian function centred on the measured value, and with  $\sigma$  equal to the flux uncertainties. The performance of the new redshift estimation and the redshift of the pipeline are analysed in Appendix B.

Following the selection made by Kocevski et al. (2024), we selected objects with

$$\begin{cases} \beta_{\text{opt}} > 0, \\ \beta_{\text{UV}} < -0.37, \\ \beta_{\text{UV}} > -2.8. \end{cases} \quad (2)$$

The third cut to the UV slope was applied to remove contamination by brown dwarfs. These near-IR colours of these objects are similar to those of reddened AGNs, but they appear to be significantly bluer at shorter wavelengths (Langeroodi & Hjorth 2023). To ensure a v-shape SED when the two longest wavelength filters had  $S/N > 3$ , we also requested that the flux of the filter at the longest wavelength was the highest.

In order to select only compact sources, we considered sources with  $\mu_{\text{max}} - m_{\text{point-like}} < -2.6 \text{ mag arcsec}^{-2}$ , which corresponds to the difference between the peak surface brightness ( $\mu_{\text{max}}$ ) above the background in the detection band ( $I_E$  for VIS-detected objects and  $J_E + Y_E + H_E$  for NISP-detected objects) and the expected magnitude for point-like sources ( $m_{\text{point-like}}$ ). The chosen threshold was optimised in the *Euclid* pipeline to select compact objects, such as stars (Euclid Collaboration: Romelli et al. 2025).

A red rest-frame optical continuum can be mimicked by strong nebular emission lines. We therefore performed an additional selection to remove such objects. In particular, the  $H\alpha + [\text{N II}]$  complex is present in the  $Y_E$  filter at  $z = 0.44\text{--}0.85$ , in the  $J_E$  filter at  $z = 0.77\text{--}1.39$ , in the  $H_E$  filter at  $z = 1.31\text{--}2.09$ , and in the IRAC1 filter at  $z = 3.82\text{--}4.99$ . In these redshift intervals, we imposed that the flux of the contaminated band was lower than the flux of the next redward filter. A negative slope would indeed indicate strong nebular emission lines even when the overall optical slope is consistent with our LRD slope selection. Many previous JWST samples did not perform this selection, and the LRD optical colours may indeed be boosted by nebular emission lines (Hainline et al. 2024). A more complex analysis, which we leave for future studies, is necessary to understand whether the underlying continuum of these strong-line emitters is anyway consistent with the LRD selection, however.

We then studied the distribution of the  $\chi^2$  and removed any object with  $\chi^2 \geq 100$ . This threshold was chosen based on the overall distribution of  $\chi^2$  and on a random selection of SED.

Finally, because the number of sources is limited, we visually verified the *Euclid* and IRAC cutouts of any remaining object to remove cases that were affected by blending issues in the IRAC bands, any remaining artefacts, or sources that were extended in the NISP filters. Future work that performs a detailed deblending analysis might improve over this step. This selection unfortunately removes potential close pairs, which some LRDs may be part of (e.g. Tanaka et al. 2024 found three dual LRD candidates over  $0.54 \text{ deg}^2$ ).

We also considered the photometric redshift estimation derived for NISP-detected sources that extend the redshift boundary at  $z > 6$ . As for the previous sample, we only selected reliable sources using the flagging available in the catalogue. We imposed a detection in the IRAC filters, an  $S/N > 3$  in at least four bands, and only selected v-shaped and compact sources. The sources that we selected in the different steps are listed in Table 3, but we finally did not obtain any additional LRD candidates.

The search for LRDs at  $z = 1\text{--}2.1$  can be performed without the IRAC filters because the  $J_E$  and  $H_E$  filters cover the rest-frame optical continuum (see Fig. 1). We therefore repeated the selections described above and limited the analysis to objects with a pipeline redshift  $z_{\text{pipeline}} < 3$  as a conservative cut, but removed any object that was detected in IRAC. As for the previous selection, we searched for objects that were detected in at least four filters (two blueward and two redward  $\lambda_{\text{break}}$ ), with a v-shaped continuum, which were compact, had no evident contamination from strong nebular emission lines, and with  $\chi^2 < 100$ . We visually inspected the *Euclid* cutouts of any remaining object to remove any remaining artefact or extended objects.

The final sample of LRD candidates includes 29 objects with IRAC detections. This corresponds to a density of  $0.8 \text{ deg}^{-2}$ . It also includes 3312 objects without IRAC detections and is limited to  $z \leq 2.1$ , corresponding to a density of  $57.3 \text{ deg}^{-2}$ . The total sample includes 3341 LRD candidates. The number of LRD candidates is conservative because of the uncertainties in the rest-frame UV and optical slopes we outlined in Appendix C and the conservative selection steps we performed. The complete list of LRD candidates and their properties is reported in Table D.1, and the cutouts and photometric fit of two LRDs are shown as examples in Figs 2 and 3. The *Euclid* point-spread function (PSF) is slightly undersampled in  $I_E$  has a pixel scale of  $0''.1$  and an FWHM= $0''.158\text{--}0''.164$  Euclid Collaboration: McCracken et al. (2025), which is reflected in the cutouts. The NISP images were instead interpolated to the same pixel scale as  $I_E$ , but their pixel scale originally is  $0''.3$  and their FWHM= $0.35''$ .

The redshift and magnitude distributions in the three fields are reported in Appendix E. They show that the selection is reasonably uniform across the fields.

### 3.2. Differences between the IRAC-detected and IRAC-undetected LRD candidates.

The difference in density of LRD candidates with and without IRAC is probably driven by several factors. On the one hand, the number of LRD candidates with IRAC may be underestimated because blending issues can affect IRAC fluxes. This produces a boost in the contaminated band that results in a large  $\chi^2$ , and we simultaneously performed a stricter visual check to remove any possible blended source. As shown in Table 3, the fraction of sources removed by the  $\chi^2$  cut and the visual inspection is

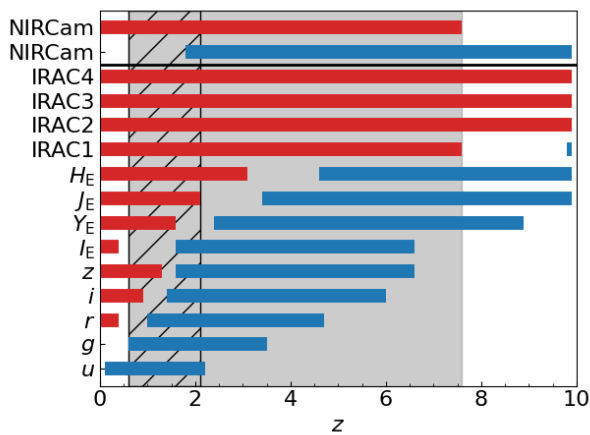


**Fig. 1.** Redshifts in which the different *Euclid*, IRAC, and ground-based filters trace the optical (red bars) or UV (blue bars) continuum. The grey shaded area indicates the redshift range in which we have at least four filters to derive the slopes necessary to select LRDs. The hatched area indicates the redshift range covered without IRAC. The first two bars, separated by a horizontal solid black line, indicate the redshift range in which at least two JWST NIRCcam broad-band filters trace the rest-frame optical or UV continuum.

larger for IRAC-detected sources. To understand the importance of blending, we verified that about 15% of all reliable *Euclid* sources had a neighbour within  $2''$  (equal to the smallest IRAC FWHM) and that 5% of the sources had a neighbour within  $1''$ . LRDs might cluster more strongly at kiloparsec scales (Tanaka et al. 2024), and the effect of blending might therefore be even stronger in LRDs than in the general galaxy population. In addition, the FWHM of IRAC is larger than the radius we used for the photometry, so that flux loss might effect the source detection.

On the other hand, the number of LRD candidates selected without IRAC may be overestimated because the  $H\alpha + [\text{N II}]$  complex is contained within the  $H_E$  filter at  $z = 1.31\text{--}2.09$ . The IRAC bands can help us to identify them. In addition, the wider wavelength coverage can simply improve the removal of any type of contaminants.

Some differences may be intrinsic, however. Observations with the JWST mid-infrared instrument (MIRI) have shown that the rest-frame continuum at  $\lambda \gtrsim 0.7\ \mu\text{m}$  becomes remarkably flat. This indicates a mild contribution from an obscured AGN (Williams et al. 2024; Pérez-González et al. 2024) or an AGN torus without hot dust (Leung et al. 2024; Barro et al. 2024). At  $z < 2.8$ , IRAC bands cover the same rest-frame wavelengths as MIRI at  $z > 5$  (i.e.  $\lambda \gtrsim 0.7\ \mu\text{m}$ ). This covers the flatter part of the SED.

## 4. Results

### 4.1. Comparison with the JWST LRD catalogues

In Fig. 4 we show a comparison of the redshift and  $M_{\text{UV}}$  at  $1450\ \text{\AA}$  of our sample of LRD candidates, derived by fitting the available data with two power laws, as explained in detail in Appendix B. We also compare our results with some of the previous samples derived with JWST data (Kocevski et al. 2024; Labbé et al. 2023; Kokorev et al. 2024a). Our sample is complementary to the JWST samples that were derived so far because it covers brighter magnitudes. Only one JWST source is as bright as *Euclid*-selected sources. It is also clear that our sample extends to lower redshifts than the JWST sample. In the same figure, we also show the  $M_{\text{UV}}$  that we expect to reach at the end of the *Eu-*

**Table 4.** FWHM of the *Euclid* VIS/NISP, JWST NIRCcam, and IRAC PSFs.

Filter	FWHM		
	[arcsec]	[kpc] at $z = 1$	[kpc] at $z = 6$
<i>Euclid</i> / $I_E$	0.16	1.3	0.9
<i>Euclid</i> / $H_E$	0.3	2.5	1.8
JWST/F070W	0.029	0.2	0.17
JWST/F150W	0.050	0.4	0.29
JWST/F356W	0.116	0.96	0.67
JWST/F444W	0.145	1.19	0.85
IRAC/IRAC1	1.66–1.95 <sup>a</sup>	13.7–16.1	9.7–11.4
IRAC/IRAC2	1.72–2.02 <sup>a</sup>	14.2–16.6	10.0–11.8

**Notes.** Citations: *Euclid*/ $I_E$  (Euclid Collaboration: McCracken et al. 2025), *Euclid*/ $H_E$  (Euclid Collaboration: Polenta et al. 2025). JWST (Rigby et al. 2023). <sup>a</sup> The two numbers refer to when *Spitzer* was cryogenically cooled and when it was warm, respectively.

*clid* mission. The EDFs will be two magnitudes deeper when completed. Even when the IRAC data remain unchanged, this will allow us to reach  $M_{\text{UV}} = -20$  at  $z = 4$ , which extends the overlap with JWST, but also probes the bright end up to  $z = 8$ .

It is necessary, however, to consider that even if we select only compact sources, the different angular resolution of JWST and *Euclid* might affect the selection. In Table 4 we report the FWHM of the two missions at similar wavelengths, with the corresponding physical scales given at  $z = 1$  and  $z = 6$ . The difference with respect to IRAC is even larger and reaches a factor of at least 10 in physical size. Therefore, follow-up campaigns will be necessary to confirm that the LRD candidates identified with *Euclid* and IRAC are as compact as the JWST candidates.

To understand the level of contamination from the different angular resolutions of JWST and *Euclid*, we analysed the subsample of extended v-shape sources from Kocevski et al. (2024, priv. com.). These sources are mainly dusty star-forming galaxies and correspond to 14% of all v-shape sources, but their redshift distribution is skewed toward  $z < 4$  (see Fig. 7 in Kocevski et al. 2024). In Fig. 5 we compare the size of these extended v-shape sources derived from the JWST/F444W filter with the angular resolution of *Euclid*. In particular, the JWST/F444W filter and the  $H_E$  filter both trace the rest-frame optical of the LRDs up to  $z = 3.1$  and can therefore be compared directly. This comparison clearly shows that the majority of these sources are also extended for *Euclid*. Only 8% (15) of them are below the  $H_E$  filter FWHM at  $z = 2\text{--}4$ . Combining this finding with the redshift distribution of the LRD candidates by Kocevski et al. (2024), we obtained that we expect 15% of contaminants at  $z = 2\text{--}4$ .

At lower redshift, these contaminants are expected to contribute even less, but we do not have direct measurements because the sample by Kocevski et al. (2024) is limited to  $z > 2$ . Considering the redshift evolution of the size mass relation for late-type galaxies (van der Wel et al. 2014), however, we expect a median increase in the galaxy size by 1.2 between  $z = 2.25$  and  $z = 1.75$  and 1.9 between  $z = 2.25$  and  $z = 0.75$ . The smallest extended v-shape source at  $z < 4$  by Kocevski et al. (2024) is only a factor of 0.88 of the *Euclid* angular resolution in the  $H_E$  band. We therefore expect that all sources at  $z < 2$  are resolved.

### 4.2. Comparison with other *Euclid* AGN catalogues

Other works have focused on the selection of AGNs and mainly used Q1 photometric data. We therefore investigated the amount

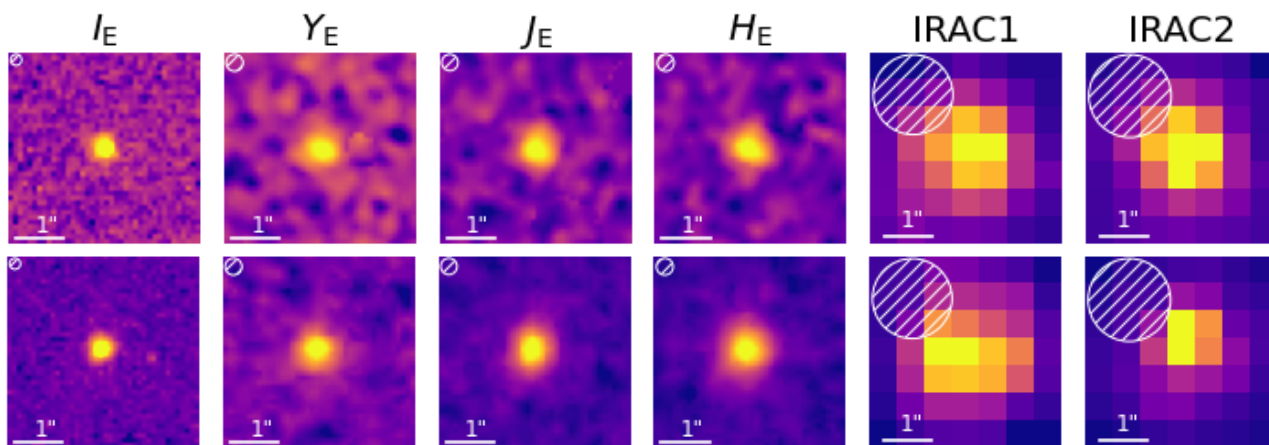


**Fig. 2.** Two example LRD candidates, showing cutouts of  $4'' \times 4''$  in the four *Euclid* filters and the two shortest IRAC channels. From left to right:  $I_E$ ,  $Y_E$ ,  $J_E$ ,  $H_E$ , IRAC1, and IRAC2. We report the size of the PSF in the top left and the physical scale on the bottom left corner of each panel.

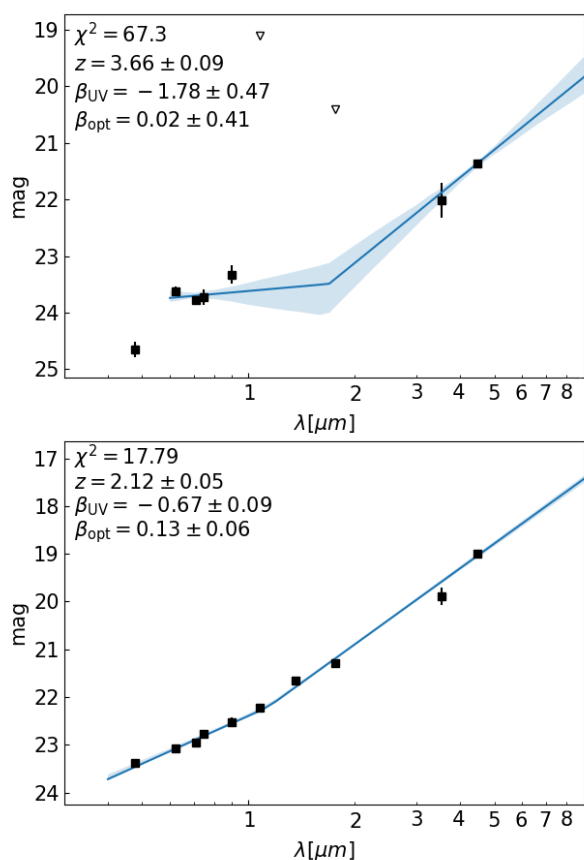


**Fig. 3.** Fit with two power-laws of the photometric data of the two example LRD candidates shown in Fig. 2. We show fluxes with  $S/N > 3$  as black squares, and the  $3\sigma$  upper limits are shown with empty triangles. The best fit is shown with a blue solid line, and the shaded region shows the 16% and 84% uncertainties. We report the  $\chi^2$  and the output parameters in the top left corner.

of overlap with our sample of LRD candidates. In particular, the *Euclid* AGN catalogue presented by [Euclid Collaboration: Mataro Zatarain et al. \(2025\)](#) focused on the selection of AGN, mainly blue QSOs, based on *Euclid* photometry, but also on ancillary data from UV to IR, and previous public spectroscopic data. [Euclid Collaboration: Roster et al. \(2025\)](#) instead matched *Euclid* sources with public X-ray surveys and identified X-ray

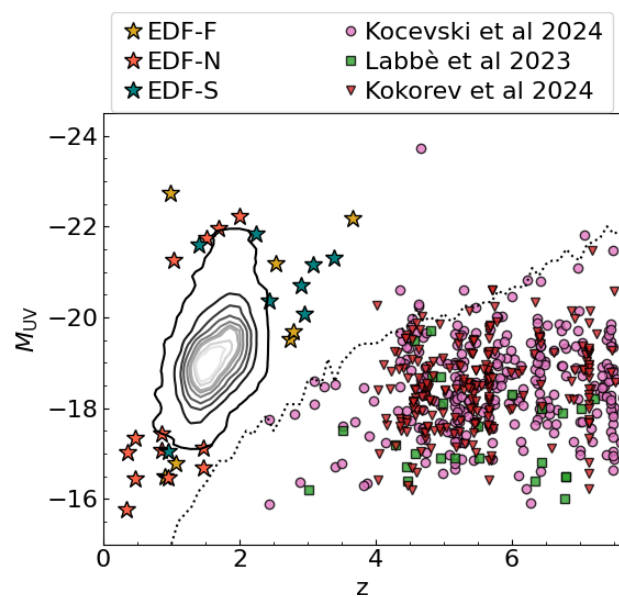


**Fig. 4.**  $M_{UV}$  and redshift for all LRD candidates, shown as contour lines, equally spaced from 10% to 90%. The last line represents 99% of the distribution. The remaining 1% of the sample is shown with stars, colour-coded based on their field. We also show three samples of LRDs selected with JWST observations ([Kocevski et al. 2024](#); [Labbé et al. 2023](#); [Kokorev et al. 2024a](#); [Akina et al. 2024](#)). The dotted black line shows the 80% completeness that is expected when the EDFs are at their final depth.

detected AGNs. The details of these selections and the overlap with our samples of LRD candidates is reported in [Appendix F](#). No sources are identified by all QSO selections in de EDF-F and EDF-S overall, and 1898 (80%) are selected by at least one criterion. In the EDF-N, 816 sources, which corresponds to 84% of the EDF-N sample of LRD candidates, is selected by at least one QSO criterion, while no sources are selected by all criteria.

#### 4.3. LRDs luminosity function

To measure the UV luminosity function of our sample of LRD candidates, we used the  $1/V_{\max}$  method ([Rowan-Robinson 1968](#); [Schmidt 1968](#)). In particular, the luminosity for each magnitude

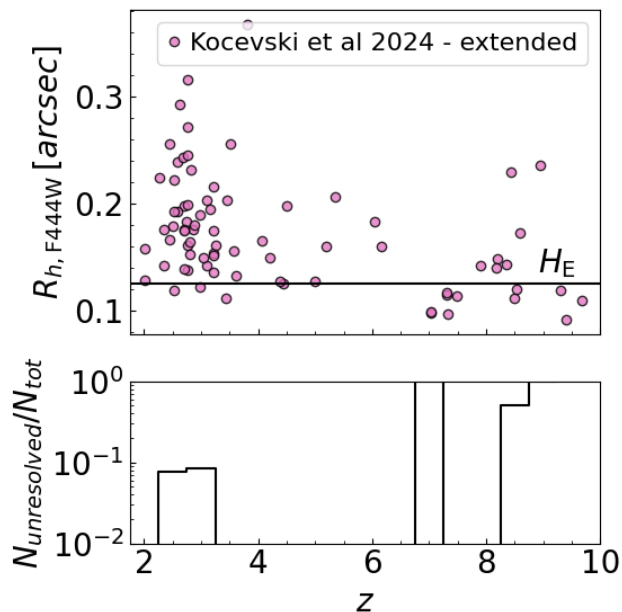


**Fig. 5.** Top: Half-light ratio in the JWST/F444W filter vs. redshift for the sample of extended v-shape objects by Kocevski et al. (2024). The horizontal solid line indicate the  $H_E$  band FWHM, scaled assuming a Gaussian function. Bottom: Fraction of extended v-shape objects that is expected to be unresolved in the  $H_E$  band as a function of redshift.

550 and redshift bin is defined as

$$\Phi(M)dM = \frac{1}{\Delta M} \sum_i^N \frac{1}{w_i V_{\max,i}}, \quad (3)$$

where  $\Delta M$  is the width of the magnitude bin,  $w_i$  is the completeness correction for the  $i$ th object, and  $V_{\max,i}$  is the maximum comoving volume at which object  $i$  could have been detected. To calculate the latter, we considered the area that is covered by the observations, the minimum redshift of the bin, and the maximum redshift at which each source could be observed. The latter was derived considering the v-shaped model of each source, described by two power laws with slopes  $\beta_{UV,i}$  and  $\beta_{opt,i}$ , normalised to the absolute UV magnitude ( $M_{UV,i}$ ). This model was then shifted from the minimum to the maximum redshift of the redshift bin and was convolved at each redshift step with the *Euclid* and ancillary bands to estimate the expected fluxes. These fluxes were then used to derive the maximum redshift at which we would have at least four filters with  $S/N > 3$ .

#### 565 4.3.1. Area

The area associated with each field was derived considering the coverage map for the four *Euclid* filters, combined to remove the area in which at least one filter was masked. In addition, we also removed additional masked areas that covered bright stars, both halo and ground-bleeding trails, and extended bright foreground sources. In addition, we combined these masks with the coverage by IRAC to derive the area associated with IRAC-detected sources. The areas we considered are listed in Table 5.

#### 4.3.2. Completeness limits and correction

575 To derive the 80% completeness limit of our sample, we derived the fraction of LRDs with at least four filters with  $S/N > 3$  as a function of redshift and  $M_{UV}$ . In particular, we considered

**Table 5.** Area in  $\text{deg}^2$  used to estimate the LRD luminosity function.

	EDF-F	EDF-N	EDF-S
After masking	11.85	19.76	26.16
w/IRAC	2.57	13.46	21.10

redshift bins of  $\Delta z = 0.25$  up to  $z = 6$ , since no LRDs are found at higher redshifts. We also considered magnitude bins of  $\Delta M_{UV} = 0.25$  from  $M_{UV} = -25$  to  $M_{UV} = -10$ . In each redshift-magnitude bin, we randomly extracted 1000  $\beta_{UV}$  and  $\beta_{opt}$  values from the observed distribution. We then derived the fraction of these mock LRDs that were observed in at least four filters with  $S/N > 3$ , considering the depths of the different fields reported in Table 1. We used this estimate to correct the derived luminosity function.

We also applied the corrections for incorrect redshifts that we derived from the analysis of the redshift recovery on the simulated sample in Appendix B. This correction varied from 0.6 for  $z = 1-1.5$  because the number of sources in this redshift range is expected to be overestimated, to 1.3 for  $z = 2-2.5$ , where the number of objects is underestimated instead. A more detailed completeness correction that takes the compactness of the sources into account, for example, will be estimated in future works when the systematic effects of the telescope are understood better.

Finally, we considered a correction of 15% due to the contamination by extended sources that are unresolved by *Euclid* (see Sect. 4.1). This contamination is expected to increase at  $z > 6$ , but we found no LRD candidates at these high- $z$  values. At the same time, this correction is expected to decrease at  $z < 2$  due to the average increase of galaxy size with decreasing redshift, but we lack the data to properly quantify this decrease. As a conservative approach, we therefore applied the same correction at all redshifts.

#### 4.3.3. Uncertainties

We estimated the uncertainties of the luminosity function by performing a bootstrap analysis of the sample. We generated 100 random samples starting from the entire LRD sample. In every realisation, we also randomised the redshift and the absolute UV magnitude considering a Gaussian function centred on the best-fit value and with a standard deviation equal to their respective uncertainties. We added the Poisson errors in quadrature to these uncertainties, following the prescription by Gehrels (1986). We did not include any uncertainty due to cosmic variance because the areas we analysed are so large.

#### 4.3.4. Estimated luminosity functions

We derived the UV luminosity functions of LRDs as explained in the previous sections and considering the following redshift bins:  $0.6 \leq z < 1.0$ ;  $1.0 \leq z < 1.5$ ;  $1.5 \leq z < 2.0$ ;  $2.0 \leq z < 2.5$ ; and  $2.5 \leq z < 4.0$ . In the first redshift bin, we only considered objects in EDF-N because the other fields lack the  $u$ -band observations necessary to properly trace the UV slope. Eleven objects (0.3% of the sample) were not considered in the UV luminosity functions because they correspond to a redshift at which the UV slope is not properly covered. The derived UV luminosity functions are shown in Fig. 6, where we also compare our results with UV luminosity functions from the literature of LRDs based on JWST data (Kokorev et al. 2024a; Kocevski et al. 2024) and

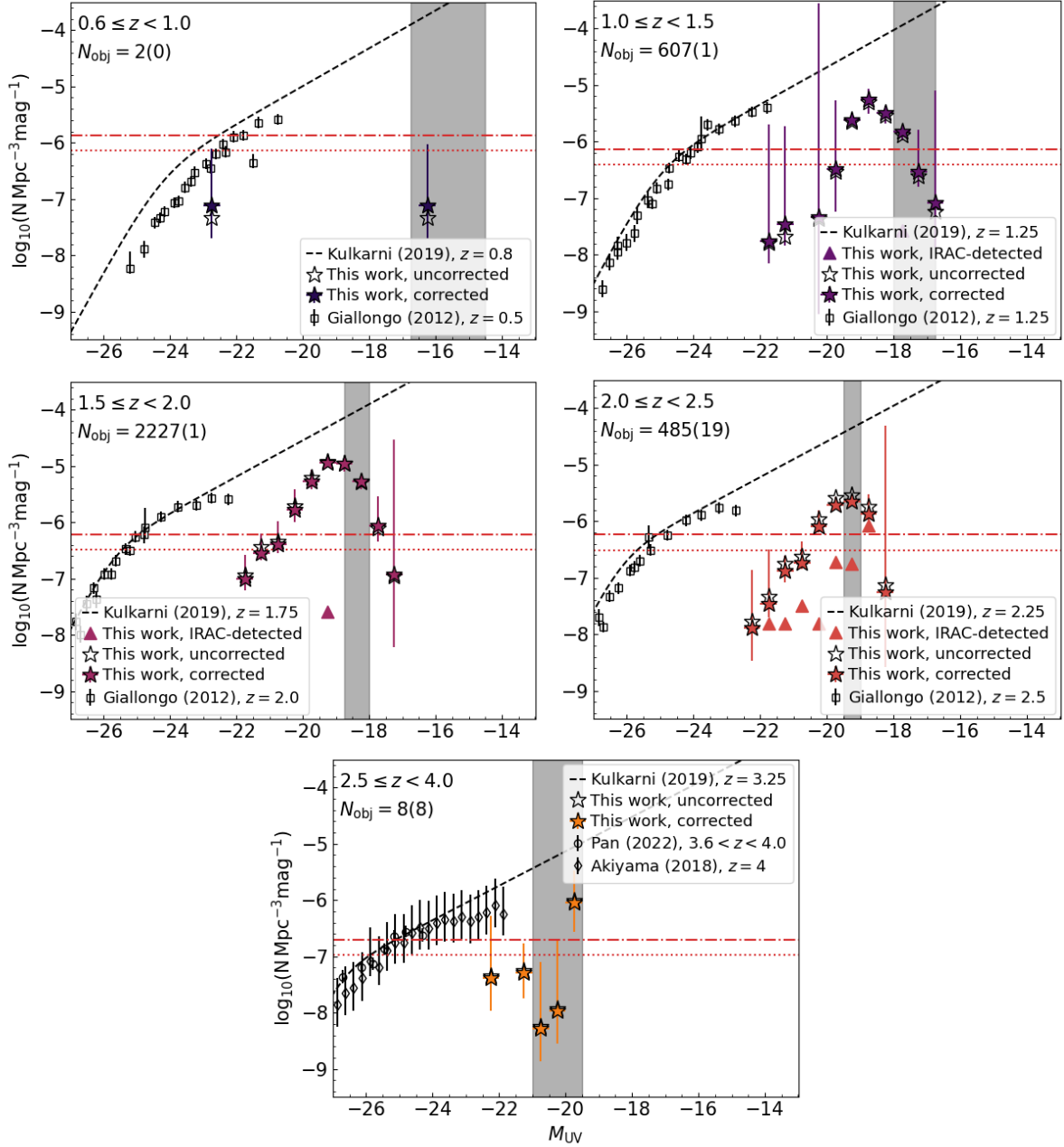


**Fig. 6.** UV luminosity function of the LRD candidates from  $z = 0$  (top left) to  $z = 4$  (bottom right). The empty stars indicate the values before any corrections, and the coloured stars show the density after correcting for completeness and redshift estimation. The coloured triangles show the conservative estimation derived considering only IRAC-detected sources. The vertical shaded black regions show the range of the 80% completeness in the three fields. In the top left corner, we report the number of objects inside the redshift bin, and we show the number of IRAC-detected sources in the bin in brackets. The empty symbols show UV luminosity functions of QSOs from Giallongo et al. (2012), and reference therein), Akiyama et al. (2018), and Pan et al. (2022). We also report the UV luminosity function of QSOs modelled by Kulkarni et al. (2019), dashed black line). For a comparison, the horizontal dash-dotted red line shows the minimum density probed by the HST CANDELS survey (0.29 deg<sup>2</sup> Grogin et al. 2011; Koekemoer et al. 2011), and the horizontal dotted red line shows the minimum density probed by the JWST COSMOS-WEB survey (0.54 deg<sup>2</sup> Casey et al. 2023).

630 QSOs, including JWST data (Maiolino et al. 2024b; Harikane  
et al. 2023; Grazian et al. 2024) or before JWST (Giallongo  
et al. 2012; McGreer et al. 2013; Giallongo et al. 2015; Akiyama  
et al. 2018; Niida et al. 2020; Pan et al. 2022). The values of  
the LRD luminosity function of this work are also reported  
635 in Table 6. When these results are analysed, it is necessary to  
consider that the luminosity function based on *Euclid* data alone  
may be overestimated because some contaminants might not

have been properly included in the corrections. On the other  
hand, the luminosity function based on IRAC observations  
might be severely underestimated because we strictly removed  
640 any source that was affected by blending.

In the highest-redshift bin (i.e.  $4.0 \leq z < 6.0$ ), we found  
no candidates. This prevents comparisons with previous JWST  
results. We must therefore wait for future *Euclid* releases to im-  
645

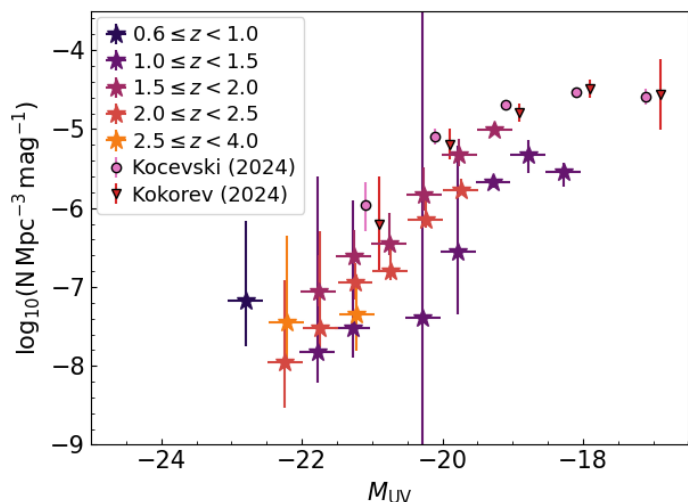


**Fig. 7.** Comparison of the corrected UV luminosity function of LRD candidates from  $z = 0$  to  $z = 4$ , and values at  $z = 6$  from the literature (Kocevski et al. 2024; Kokorev et al. 2024a).

prove over these results. The depth of the EDFs is expected to increase by two magnitudes until the end of the mission (Euclid Collaboration: Mellier et al. 2025). We predict that with the final depths of the EDFs, *Euclid* will be able to observe the brightest LRDs observed by JWST so far (Fig. 4).

At redshifts  $z < 4$ , we can only compare our results to previous QSO UV luminosity functions because observations of LRDs with JWST were mainly limited to  $z > 4$ . The luminosity function of the LRDs is always well below the QSO luminosity functions at bright magnitudes by 1.2–2.6 dex, which corresponds to 1–4 $\sigma$  because of the low number statistics, however. This difference generally indicates that LRDs are not the dominant AGN population at these magnitudes at  $z < 4$ , assuming they are AGNs. The LRD luminosity functions are instead closer to the QSO luminosity functions at  $z > 1$  and at the faintest magnitudes probed by this work. The closest point is at  $1.5 \leq z < 2.0$ , where the LRD luminosity function is only 0.7 dex below the QSO luminosity function about  $M_{UV} = -19.25$  mag, but given the large statistics, the uncertainties are small, and this difference corresponds to more than 10 $\sigma$ . We cannot verify whether the LRD luminosity function is closer to the QSO luminosity function at even fainter magnitudes because of incompleteness.

In the same figure, we also report the maximum volume probed by one of the largest JWST survey so far, that is, COSMOS-Web (Casey et al. 2023), which covers  $0.6 \text{ deg}^2$  (dotted red line in Fig. 6), and the Cosmic Assembly Near-infrared Deep Extragalactic Legacy Survey (CANDELS Grogan et al. 2011; Koekemoer et al. 2011), which covers  $0.29 \text{ deg}^2$  with the *Hubble* Space Telescope (HST; dash-dotted red line in Fig. 6). At  $z < 1$  and  $z > 2.5$ , the area of these two surveys is too small to observe a significant number of objects with luminosities similar to the candidates we selected. We would expect to observe some objects at the other redshifts, however:  $17^{+8}_{-7}$  at  $1.0 \leq z < 1.5$ ;  $62^{+16}_{-16}$  at  $1.5 \leq z < 2.0$ ; and  $15^{+4}_{-5}$  at  $2.0 \leq z < 2.5$  in CANDELS;  $31^{+15}_{-13}$  at  $1.0 \leq z < 1.5$ ;  $116^{+30}_{-30}$  at  $1.5 \leq z < 2.0$ ; and  $29^{+7}_{-8}$  at  $2.0 \leq z < 2.5$  in COSMOS-Web. At these redshifts, however, no LRD was identified with HST and only a few were identified with JWST. For example, Kocevski et al. (2024) found 17 LRD candidates at  $z < 4$ . Based on the LRD luminosity function we found here, we would expect  $56^{+11}_{-10}$  candidates in this area.

This difference (2 $\sigma$  deviation) in number density may be due to contaminants or to the different angular resolution of *Euclid* and JWST. This means that future follow-up studies are fundamental. It is important to note, however, that the number density of the subsample of more robust LRD candidates, which are those that are also observed by IRAC, is too low to be detected by any JWST or HST survey.

We also report the conservative luminosity function derived with the IRAC-detected sources alone, which have more constraints, but were also cleaned more severely to avoid blending issues. This estimates are compatible with the few LRD candidates at  $z < 4$  that were observed by JWST and HST.

A comparison between the LRDs UV luminosity functions we derived is shown in Fig. 7. This plot shows a tentative evolution of the luminosity function with redshift. The density of LRD candidates increases from the high redshift to  $z = 1.5$ – $2.5$  and decreases at even lower redshifts. For example, at  $1.5 \leq z < 2.0$  and  $M_{UV} = -20.25$  mag, we obtained a density of  $\log_{10}(N \text{ Mpc}^{-3} \text{ mag}^{-1}) = -5.83^{+0.35}_{-0.20}$ . Our estimate at the same magnitude but at  $2.0 \leq z < 2.5$  is slightly lower, that is  $\log_{10}(N \text{ Mpc}^{-3} \text{ mag}^{-1}) = -6.15^{+0.32}_{-0.10}$ , but it may be incomplete given the necessity of using IRAC data at  $z > 2.1$ . In contrast, the drop at  $z < 1.5$  is not linked to observational biases because we expect *Euclid* data to have the same capacity of selecting LRDs down to  $z = 0.7$ . To give a more quantitative estimate, at  $M_{UV} = -19.25$  mag, the LRD density is  $\log_{10}(N \text{ Mpc}^{-3} \text{ mag}^{-1}) = -5.67^{+0.07}_{-0.07}$  at  $1.0 \leq z < 1.5$  and it is  $\log_{10}(N \text{ Mpc}^{-3} \text{ mag}^{-1}) = -5.01^{+0.02}_{-0.06}$  at  $1.5 \leq z < 2.0$ , with a drop of 0.67 dex. The statistics in the lowest-redshift bin are quite poor because it is based on the EDF-N alone. This prevents us from further exploring the possible redshift evolution. The density of LRD candidates with  $M_{UV} \geq -21$  mag at  $1 \leq z < 2.5$  is also similar to the density derived with JWST at  $4 \leq z < 6$  (Kocevski et al. 2024; Kokorev et al. 2024a), however, which is  $\log_{10}(N \text{ Mpc}^{-3} \text{ mag}^{-1}) = -5.19 \pm 0.20$  and  $\log_{10}(N \text{ Mpc}^{-3} \text{ mag}^{-1}) = -5.10 \pm 0.1$  respectively. This supports the idea that the high- $z$  evolution might be due to incompleteness in our LRD sample. This evolution is absent when we only consider the few LRD candidates that were detected in IRAC because the statistics is too low.

Overall, we speculate that the LRD number density seems to remain constant from  $z = 4$ – $6$  to  $z = 1.5$ – $2.5$ , and this resembles the observed evolution of the star formation rate density (e.g. Madau & Dickinson 2014; Gruppioni et al. 2020; Traina et al. 2024), the BH accretion rate density (e.g. Delvecchio et al. 2014), and the evolution in the molecular gas mass (see Tacconi et al. 2020, for a review). When we consider that LRDs may be very dense and dust-obscured starbursts or obscured SMBHs that might accrete at a super-Eddington rate, their frequency might follow the trend for the more general population of star-forming galaxies or AGNs, which is at the end regulated by the availability of cold gas.

Further analysis is needed to understand the level of contamination in our sample or why these LRD candidates have been missed by previous JWST studies. These sources might also not be as compact as those that are observed with JWST, which are compact when the spatial resolution of *Euclid* is considered, but not with JWST, which is 4–6 times better than the *Euclid*'s. Following the estimates from Sect. 4.1 we considered 15% of such contaminants in estimating the luminosity function, but detailed spectroscopic follow-ups are necessary to properly quantify the purity of our sample of LRD candidates. If the sample is dominated by contaminants, considering that the number densities

seems to remain similar from  $z = 6$  to  $z = 2$ , we might be following different evolutionary stages of the same galaxy population.

As the depth of the EDFs increases and the spectroscopic coverage improves, the identification of LRDs and the estimation of their properties will improve in the future. This will enable us to derive more conclusive results on the possible redshift evolution of the LRD luminosity function.

## 5. Conclusions

We have taken advantage of the *Euclid* Q1 data that cover about  $63 \text{ deg}^2$  to search for LRD candidates. The selection was performed by exploiting *Euclid* photometric data, ground-based ancillary data, and Spitzer/IRAC data. After a conservative selection that included conservative flagging and a visual inspection of all candidates, we obtained a final sample of 3341 LRD candidates, 29 of which are also detected with IRAC.

Even when we imposed a  $S/N > 3$  in at least four filters, LRD candidates are relatively faint, with mean magnitudes of  $I_E = 25.5$ ,  $Y_E = 24.3$ ,  $J_E = 24.0$ , and  $H_E = 23.7$ . These are fainter than the  $5\sigma$  limits of the Q1 data release. Their photometric redshift was estimated to range between  $z = 0.33$  and  $z = 3.6$ , where previous JWST selections identified a rapid decline in the number of LRD candidates. At  $z > 4$ , the depth of the ancillary IRAC data limits our sample to only the brightest sources, however.

We also derived the rest-frame UV luminosity function, but found no overlap in the parameter space of *Euclid* and JWST. This limited the direct comparison. *Euclid* is complementary to JWST observations because it can probe the bright end of the UV luminosity function because the covered area is so large. The most puzzling result is that the UV luminosity function of LRD candidates increases from high  $z$  to  $z = 1.5\text{--}2.5$ , below which it decreases again. This is in contrast with previous JWST results, which derived a drastic drop in LRDs at  $z < 4$ , with almost no candidates at  $z < 2$ . The  $z > 4$  evolution of our luminosity function may be affected by incompleteness in our LRD candidate sample, however. It is important to note that no significant evolution is apparent in the subsample of more robust LRD candidates that are also detected by IRAC, which has poor statistics (only 29 objects), however, and is limited by the IRAC resolution. Clearly, more observations are required to clarify this situation. Another interesting result is that the LRD UV luminosity function remains below the QSO luminosity function, except at  $M_{UV} > -21$ , where they become compatible. This might indicate that if LRDs are indeed AGNs, they are a sub-dominant AGN population.

Further analyses are necessary to validate the LRD candidates of this work and optimise the removal of possible contaminants. In addition, further critical studies need to probe their structure and determine their compatibility with JWST sources because of the different spatial resolution of the two telescopes. If a sizeable fraction of the LRD candidates we identified are confirmed by future studies, it will enable us to study the redshift evolution over a broad redshift and luminosity range. This will help us to shed light on these mysterious sources. Future *Euclid* data releases are expected to increase the number of LRD candidates, but also to increase the overlap in parameter space with previous JWST samples, as the *Euclid* Wide survey will be wider than the Q1 at similar depth, while the *Euclid* Deep survey will be considerably deeper. In addition, a direct comparison between JWST and *Euclid* selections will be possible in future releases because *Euclid* will cover some of the area that was already observed with JWST.

**Data availability:** Table D.1 is only available in electronic form at the CDS via anonymous ftp to cdsarc.u-strasbg.fr (130.79.128.5) or via <http://cdsweb.u-strasbg.fr/cgi-bin/qcat?J/A+A/>.

**Acknowledgements.** The research activities described in this paper were carried out with contribution of the Next Generation EU funds within the National Recovery and Resilience Plan (PNRR), Mission 4 – Education and Research, Component 2 – From Research to Business (M4C2), Investment Line 3.1 – Strengthening and creation of Research Infrastructures, Project IR0000034–“STILES – Strengthening the Italian Leadership in ELT and SKA”. This work has benefited from the support of Royal Society Research Grant RGS\R1\231450. This research was supported by the International Space Science Institute (ISSI) in Bern, through ISSI International Team project #23-573 “Active Galactic Nuclei in Next Generation Surveys”. L.B., F.R., and V.A. acknowledge the support from the INAF Large Grant “AGN & Euclid: a close entanglement” Ob. Fu. 01.05.23.01.14. A.F. acknowledges the support from project “VLT- MOONS” CRAM 1.05.03.07, INAF Large Grant 2022 “The metal circle: a new sharp view of the baryon cycle up to Cosmic Dawn with the latest generation IFU facilities” and INAF Large Grant 2022 “Dual and binary SMBH in the multi-messenger era”. L.B. thanks A. Marasco for computational support and D. Kocevski for providing the data necessary for comparing the *Euclid* LRD candidates with the JWST ones.. This research made use of Photutils, an Astropy package for detection and photometry of astronomical sources (Bradley et al. 2023). The Euclid Consortium acknowledges the European Space Agency and a number of agencies and institutes that have supported the development of *Euclid*, in particular the Agenzia Spaziale Italiana, the Austrian Forschungsförderungsgesellschaft funded through BMK, the Belgian Science Policy, the Canadian Euclid Consortium, the Deutsches Zentrum für Luft- und Raumfahrt, the DTU Space and the Niels Bohr Institute in Denmark, the French Centre National d’Etudes Spatiales, the Fundação para a Ciência e a Tecnologia, the Hungarian Academy of Sciences, the Ministerio de Ciencia, Innovación y Universidades, the National Aeronautics and Space Administration, the National Astronomical Observatory of Japan, the Nederlandse Onderzoekschool voor Astronomie, the Norwegian Space Agency, the Research Council of Finland, the Romanian Space Agency, the State Secretariat for Education, Research, and Innovation (SERI) at the Swiss Space Office (SSO), and the United Kingdom Space Agency. A complete and detailed list is available on the *Euclid* web site ([www.euclid-ec.org](http://www.euclid-ec.org)). Based on data from UNIONS, a scientific collaboration using three Hawaii-based telescopes: CFHT, Pan-STARRS, Subaru [www.skysurvey.cc](http://www.skysurvey.cc). Based on data from the Dark Energy Camera (DECam) on the Blanco 4-m Telescope at CTIO in Chile <https://www.darkenergysurvey.org>. This work uses results from the ESA mission *Gaia*, whose data are being processed by the Gaia Data Processing and Analysis Consortium <https://www.cosmos.esa.int/gaia>. This publication is based on observations made with the Spitzer Space Telescope, which is operated by the Jet Propulsion Laboratory, California Institute of Technology under a contract with NASA, and has made use of the NASA/IPAC Infrared Science Archive, which is funded by the National Aeronautics and Space Administration and operated by the California Institute of Technology.

## References

- Abbott, T. M. C., Abdalla, F. B., Allam, S., et al. 2018, *ApJS*, 239, 18
- Akins, H. B., Casey, C. M., Lambrides, E., et al. 2024, arXiv e-prints, arXiv:2406.10341
- Akiyama, M., He, W., Ikeda, H., et al. 2018, *PASJ*, 70, S34
- Alexander, T. & Natarajan, P. 2014, *Science*, 345, 1330
- Ananna, T. T., Bogdán, Á., Kovács, O. E., Natarajan, P., & Hickox, R. C. 2024, *ApJ*, 969, L18
- Assef, R. J., Stern, D., Noirod, G., et al. 2018, *ApJS*, 234, 23
- Asthana, S., Haehnelt, M. G., Kulkarni, G., et al. 2024, arXiv e-prints, arXiv:2409.15453
- Atek, H., Labbé, I., Furtak, L. J., et al. 2024, *Nature*, 626, 975
- Baggen, J. F. W., van Dokkum, P., Brammer, G., et al. 2024, *ApJ*, 977, L13
- Barkana, R. & Loeb, A. 2001, *Phys. Rep.*, 349, 125
- Barro, G., Perez-Gonzalez, P. G., Kocevski, D. D., et al. 2024, arXiv e-prints, arXiv:2412.01887
- Barro, G., Perez-Gonzalez, P. G., Kocevski, D. D., et al. 2023, arXiv e-prints, arXiv:2305.14418
- Begelman, M. C. & Volonteri, M. 2017, *MNRAS*, 464, 1102
- Bellovary, J. 2025, arXiv e-prints, arXiv:2501.03309
- Bisigello, L., Giuliotti, M., Prandoni, I., et al. 2025, *The Open Journal of Astrophysics*, 8
- Bradley, L., Sipőcz, B., Robitaille, T., et al. 2023, *astropy/photutils*: 1.10.0
- Carr, B. J. & Hawking, S. W. 1974, *MNRAS*, 168, 399
- Casey, C. M., Kartaltepe, J. S., Drakos, N. E., et al. 2023, *ApJ*, 954, 31
- Dayal, P. 2024, *A&A*, 690, A182

**Table 6.** UV luminosity function of LRD candidates.

$M_{UV}$	$0.6 \leq z < 1.0$	$1.0 \leq z < 1.5$	$1.5 \leq z < 2.0$	$2.0 \leq z < 2.5$	$2.5 \leq z < 4.0$
-22.75	$-7.18^{+1.01}_{-0.57}$				
-22.25				$-7.95^{+1.03}_{-0.57}$	$-7.45^{+1.1}_{-0.57}$
-21.75		$-7.82^{+2.22}_{-0.40}$	$-7.06^{+0.47}_{-0.19}$	$-7.52^{+1.23}_{-0.25}$	
-21.25		$-7.52^{+1.61}_{-0.38}$	$-6.61^{+0.34}_{-0.11}$	$-6.94^{+0.24}_{-0.22}$	$-7.35^{+0.51}_{-0.45}$
-20.75			$-6.45^{+0.39}_{-0.15}$	$-6.80^{+0.4}_{-0.12}$	$-8.34^{+1.19}_{-0.57}$
-20.25		$-7.39^{+4.01}_{-1.66}$	$-5.83^{+0.35}_{-0.20}$	$-6.15^{+0.32}_{-0.10}$	$-8.03^{+1.40}_{-0.57}$
-19.75		$-6.55^{+1.33}_{-0.80}$	$-5.33^{+0.21}_{-0.14}$	$-5.77^{+0.13}_{-0.04}$	$-6.11^{+0.58}_{-0.52}$
-19.25		$-5.67^{+0.07}_{-0.07}$	$-5.01^{+0.02}_{-0.06}$	$-5.72^{+0.10}_{-0.06}$	
-18.75		$-5.32^{+0.19}_{-0.23}$	$-5.02^{+0.11}_{-0.14}$	$-5.92^{+0.29}_{-0.11}$	
-18.25		$-5.55^{+0.12}_{-0.18}$	$-5.33^{+0.09}_{-0.14}$	$-7.32^{+2.94}_{-1.28}$	
-17.75		$-5.88^{+0.07}_{-0.15}$	$-6.12^{+0.45}_{-0.25}$		
-17.25		$-6.60^{+0.77}_{-0.27}$	$-6.98^{+2.39}_{-1.35}$		
-16.75		$-7.15^{+1.77}_{-0.59}$			
-16.25	$-7.18^{+1.07}_{-0.57}$				

**Notes.** The first column shows the central value of the UV absolute magnitude bins, which are 0.5 mag wide. The other columns show the logarithm of the number density in  $\text{Mpc}^{-3} \text{mag}^{-1}$  in different redshift bins, reported in the first row.

- 885 Dayal, P. & Ferrara, A. 2018, *Phys. Rep.*, 780, 1  
Dayal, P., Volonteri, M., Greene, J. E., et al. 2025, *A&A*, 697, A211  
Declair, M., Gordon, K. D., Andrews, J. E., et al. 2022, *ApJ*, 930, 15  
Delvecchio, I., Daddi, E., Sargent, M. T., et al. 2022, *A&A*, 668, A81  
Delvecchio, I., Gruppioni, C., Pozzi, F., et al. 2014, *MNRAS*, 439, 2736  
890 DESI Collaboration, Adame, A. G., Aguilar, J., et al. 2024, *AJ*, 168, 58  
Donley, J. L., Koekemoer, A. M., Brusa, M., et al. 2012, *ApJ*, 748, 142  
Euclid Collaboration: Aussel, H., Tereno, I., Schirmer, M., et al. 2025, *A&A*, submitted (Euclid Q1 S1), arXiv:2503.15302  
Euclid Collaboration: Bisigello, L., Massimo, M., Tortora, C., et al. 2024, *A&A*, 691, A1  
895 Euclid Collaboration: Cropper, M., Al-Bahlawan, A., Amiaux, J., et al. 2025, *A&A*, 697, A2  
Euclid Collaboration: Jahnke, K., Gillard, W., Schirmer, M., et al. 2025, *A&A*, 697, A3  
900 Euclid Collaboration: Margalef-Bentabol, B., Wang, L., La Marca, A., et al. 2025, *A&A*, submitted (Euclid Q1 S1), arXiv:2503.15318  
Euclid Collaboration: Matamoro Zatarain, T., Fotopoulou, S., Ricci, F., et al. 2025, *A&A*, submitted (Euclid Q1 S1), arXiv:2503.15320  
Euclid Collaboration: McCracken, H. J., Benson, K., Dolding, C., et al. 2025, *A&A*, accepted (Euclid Q1 S1), arXiv:2503.15303  
905 Euclid Collaboration: McPartland, C. J. R., Zalesky, L., Weaver, J. R., et al. 2025, *A&A*, 695, A259  
Euclid Collaboration: Mellier, Y., Abdurro'uf, Acevedo Barroso, J., et al. 2025, *A&A*, 697, A1  
910 Euclid Collaboration: Moneti, A., McCracken, H. J., Shuntov, M., et al. 2022, *A&A*, 658, A126  
Euclid Collaboration: Polenta, G., Frailis, M., Alavi, A., et al. 2025, *A&A*, accepted (Euclid Q1 S1), arXiv:2503.15304  
Euclid Collaboration: Romelli, E., Kümmel, M., Dole, H., et al. 2025, *A&A*, in press (Euclid Q1 S1), <https://doi.org/10.1051/0004-6361/202554588>, arXiv:2503.15305  
915 Euclid Collaboration: Roster, W., Salvato, M., Buchner, J., et al. 2025, *A&A*, accepted (Euclid Q1 S1), arXiv:2503.15316  
Euclid Collaboration: Tucci, M., Paltani, S., Hartley, W. G., et al. 2025, *A&A*, in press (Euclid Q1 S1), <https://doi.org/10.1051/0004-6361/202554588>, arXiv:2503.15306  
920 Euclid Collaboration: Zalesky, L., McPartland, C. J. R., Weaver, J. R., et al. 2025, *A&A*, 695, A229  
Euclid Quick Release Q1. 2025, <https://doi.org/10.57780/esa-2853f3b>  
925 Ferrarese, L. 2002, *ApJ*, 578, 90  
Fitzpatrick, E. L., Massa, D., Gordon, K. D., Bohlin, R., & Clayton, G. C. 2019, *ApJ*, 886, 108  
Fumagalli, M., Patel, S. G., Franx, M., et al. 2012, *ApJ*, 757, L22  
Furtak, L. J., Zitrin, A., Plat, A., et al. 2023, *ApJ*, 952, 142  
930 Gaia Collaboration: Vallenari, A., Brown, A. G. A., Prusti, T., et al. 2023, *A&A*, 674, A1  
Gebhardt, K., Bender, R., Bower, G., et al. 2000, *ApJ*, 539, L13  
Gehrels, N. 1986, *ApJ*, 303, 336  
Giallongo, E., Grazian, A., Fiore, F., et al. 2015, *A&A*, 578, A83  
Giallongo, E., Menci, N., Fiore, F., et al. 2012, *ApJ*, 755, 124 935  
Glikman, E., Simmons, B., Mailly, M., et al. 2015, *ApJ*, 806, 218  
Glikman, E., Urrutia, T., Lacy, M., et al. 2012, *ApJ*, 757, 51  
Gordon, K. D., Cartledge, S., & Clayton, G. C. 2009, *ApJ*, 705, 1320  
Gordon, K. D., Clayton, G. C., Declair, M., et al. 2023, *ApJ*, 950, 86  
Gordon, K. D., Misselt, K. A., Bouwman, J., et al. 2021, *ApJ*, 916, 33 940  
Grazian, A., Giallongo, E., Boutsia, K., et al. 2024, *ApJ*, 974, 84  
Greene, J. E., Labbe, I., Goulding, A. D., et al. 2024, *ApJ*, 964, 39  
Grogin, N. A., Kocevski, D. D., Faber, S. M., et al. 2011, *The Astrophysical Journal Supplement Series*, 197, 35  
Gruppioni, C., Béthermin, M., Loiacono, F., et al. 2020, *A&A*, 643, A8 945  
Gültekin, K., Richstone, D. O., Gebhardt, K., et al. 2009, *ApJ*, 698, 198  
Habouzit, M., Li, Y., Somerville, R. S., et al. 2021, *MNRAS*, 503, 1940  
Habouzit, M., Pisani, A., Goulding, A., et al. 2020, *MNRAS*, 493, 899  
Hainline, K. N., Maiolino, R., Juodzbali, I., et al. 2024, arXiv e-prints, arXiv:2410.00100 950  
Harikane, Y., Zhang, Y., Nakajima, K., et al. 2023, *ApJ*, 959, 39  
Hawking, S. 1971, *MNRAS*, 152, 75  
Hickox, R. C. & Alexander, D. M. 2018, *ARA&A*, 56, 625  
Inayoshi, K., Haiman, Z., & Ostriker, J. P. 2016, *MNRAS*, 459, 3738  
Inayoshi, K. & Maiolino, R. 2024, arXiv e-prints, arXiv:2409.07805 955  
Juodžbalis, I., Ji, X., Maiolino, R., et al. 2024, *MNRAS*, 535, 853  
Killi, M., Watson, D., Brammer, G., et al. 2024, *A&A*, 691, A52  
Kocevski, D. D., Finkelstein, S. L., Barro, G., et al. 2024, arXiv e-prints, arXiv:2404.03576  
Kocevski, D. D., Onoue, M., Inayoshi, K., et al. 2023, *ApJ*, 954, L4 960  
Koekemoer, A. M., Faber, S. M., Ferguson, H. C., et al. 2011, *ApJS*, 197, 36  
Kokorev, V., Caputi, K. I., Greene, J. E., et al. 2024a, *ApJ*, 968, 38  
Kokorev, V., Chisholm, J., Endsley, R., et al. 2024b, *ApJ*, 975, 178  
Kokubo, M. & Harikane, Y. 2024, arXiv e-prints, arXiv:2407.04777  
Kulkarni, G., Worseck, G., & Hennawi, J. F. 2019, *MNRAS*, 488, 1035 965  
Labbe, I., Greene, J. E., Bezanson, R., et al. 2023, arXiv e-prints, arXiv:2306.07320  
Labbe, I., Greene, J. E., Bezanson, R., et al. 2025, *ApJ*, 978, 92  
Labbé, I., van Dokkum, P., Nelson, E., et al. 2023, *Nature*, 616, 266  
Langeroodi, D. & Hjorth, J. 2023, *ApJ*, 957, L27 970  
Leung, G. C. K., Finkelstein, S. L., Pérez-González, P. G., et al. 2024, arXiv e-prints, arXiv:2411.12005  
Lin, R., Zheng, Z.-Y., Jiang, C., et al. 2024, arXiv e-prints, arXiv:2412.08396  
Madau, P. & Dickinson, M. 2014, *ARA&A*, 52, 415  
Madau, P., Giallongo, E., Grazian, A., & Haardt, F. 2024, *ApJ*, 971, 75 975  
Magorrian, J., Tremaine, S., Richstone, D., et al. 1998, *ApJ*, 115, 2285  
Maiolino, R., Risaliti, G., Signorini, M., et al. 2024a, arXiv e-prints, arXiv:2405.00504  
Maiolino, R., Scholtz, J., Curtis-Lake, E., et al. 2024b, *A&A*, 691, A145  
Maiolino, R., Scholtz, J., Witstok, J., et al. 2024c, *Nature*, 627, 59 980  
Matthee, J., Naidu, R. P., Brammer, G., et al. 2024, *ApJ*, 963, 129

- Mazzolari, G., Gilli, R., Maiolino, R., et al. 2024, arXiv e-prints, arXiv:2412.04224
- McGreer, I. D., Jiang, L., Fan, X., et al. 2013, *ApJ*, 768, 105
- 985 Mezcuca, M., Pacucci, F., Suh, H., Siudek, M., & Natarajan, P. 2024, *ApJ*, 966, L30
- Mullaney, J. R., Daddi, E., Béthermin, M., et al. 2012, *ApJ*, 753, L30
- Netzer, H. 2015, *ARA&A*, 53, 365
- Niida, M., Nagao, T., Ikeda, H., et al. 2020, *ApJ*, 904, 89
- 990 Noboriguchi, A., Inoue, A. K., Nagao, T., Toba, Y., & Misawa, T. 2023, *ApJ*, 959, L14
- Oke, J. B. & Gunn, J. E. 1983, *ApJ*, 266, 713
- Pacucci, F. & Loeb, A. 2022, *MNRAS*, 509, 1885
- Pacucci, F., Natarajan, P., Volonteri, M., Cappelluti, N., & Urry, C. M. 2017, *ApJ*, 850, L42
- 995 Pan, Z., Jiang, L., Fan, X., Wu, J., & Yang, J. 2022, *ApJ*, 928, 172
- Pérez-González, P. G., Barro, G., Rieke, G. H., et al. 2024, *ApJ*, 968, 4
- Reis, I., Baron, D., & Shahaf, S. 2019, *AJ*, 157, 16
- Richards, G. T., Hall, P. B., Vanden Berk, D. E., et al. 2003, *AJ*, 126, 1131
- 1000 Rigby, J., Perrin, M., McElwain, M., et al. 2023, *Publications of the Astronomical Society of the Pacific*, 135, 048001
- Rowan-Robinson, M. 1968, *MNRAS*, 138, 445
- Salvato, M., Wolf, J., Dwelly, T., et al. 2022, *A&A*, 661, A3
- Schmidt, M. 1968, *ApJ*, 151, 393
- 1005 Silk, J. & Rees, M. J. 1998, *A&A*, 331, L1
- Simmonds, C., Tacchella, S., Hainline, K., et al. 2024, *MNRAS*, 535, 2998
- Stepney, M., Banerji, M., Tang, S., et al. 2024, *MNRAS*, 533, 2948
- Tacconi, L. J., Genzel, R., & Sternberg, A. 2020, *ARA&A*, 58, 157
- Tanaka, T. S., Silverman, J. D., Shimasaku, K., et al. 2024, arXiv e-prints, arXiv:2412.14246
- 1010 Tee, W. L., Fan, X., Wang, F., & Yang, J. 2024, arXiv e-prints, arXiv:2412.05242
- Traina, A., Gruppioni, C., Delvecchio, I., et al. 2024, *A&A*, 681, A118
- Urrutia, T., Lacy, M., & Becker, R. H. 2008, *ApJ*, 674, 80
- van der Wel, A., Franx, M., van Dokkum, P. G., et al. 2014, *ApJ*, 788, 28
- 1015 Virtanen, P., Gommers, R., Oliphant, T. E., et al. 2020, *Nature Methods*, 17, 261
- Wang, B., Leja, J., de Graaff, A., et al. 2024, *ApJ*, 969, L13
- Webster, R. L., Francis, P. J., Peterson, B. A., Drinkwater, M. J., & Masci, F. J. 1995, *Nature*, 375, 469
- Wethers, C. F., Banerji, M., Hewett, P. C., et al. 2018, *MNRAS*, 475, 3682
- 1020 Williams, C. C., Alberts, S., Ji, Z., et al. 2024, *ApJ*, 968, 34
- Wyithe, J. S. B. & Loeb, A. 2012, *MNRAS*, 425, 2892
- Yue, M., Eilers, A.-C., Ananna, T. T., et al. 2024, *ApJ*, 974, L26
- Zhang, Z., Jiang, L., Liu, W., & Ho, L. C. 2024, arXiv e-prints, arXiv:2411.02729
- 16 Institut d'Estudis Espacials de Catalunya (IEEC), Edifici RDIT, Campus UPC, 08860 Castelldefels, Barcelona, Spain 1055
- 17 Max Planck Institute for Extraterrestrial Physics, Giessenbachstr. 1, 85748 Garching, Germany
- 18 Instituto de Astrofísica de Canarias (IAC); Departamento de Astrofísica, Universidad de La Laguna (ULL), 38200, La Laguna, Tenerife, Spain 1060
- 19 Department of Astronomy, University of Geneva, ch. d'Ecogia 16, 1290 Versoix, Switzerland
- 20 Department of Physical Sciences, Ritsumeikan University, Kusatsu, Shiga 525-8577, Japan
- 21 National Astronomical Observatory of Japan, 2-21-1 Osawa, Mitaka, Tokyo 181-8588, Japan 1065
- 22 Academia Sinica Institute of Astronomy and Astrophysics (ASIAA), 11F of ASMA, No. 1, Section 4, Roosevelt Road, Taipei 10617, Taiwan
- 23 SRON Netherlands Institute for Space Research, Landleven 12, 9747 AD, Groningen, The Netherlands 1070
- 24 Kapteyn Astronomical Institute, University of Groningen, PO Box 800, 9700 AV Groningen, The Netherlands
- 25 INAF-Osservatorio di Astrofisica e Scienza dello Spazio di Bologna, Via Piero Gobetti 93/3, 40129 Bologna, Italy 1075
- 26 Sterrenkundig Observatorium, Universiteit Gent, Krijgslaan 281 S9, 9000 Gent, Belgium
- 27 STAR Institute, University of Liège, Quartier Agora, Allée du six Août 19c, 4000 Liège, Belgium
- 28 INAF-Istituto di Astrofisica e Planetologia Spaziali, via del Fosso del Cavaliere, 100, 00100 Roma, Italy 1080
- 29 Dipartimento di Fisica e Astronomia "Augusto Righi" - Alma Mater Studiorum Università di Bologna, via Piero Gobetti 93/2, 40129 Bologna, Italy
- 30 Université Paris-Saclay, CNRS, Institut d'astrophysique spatiale, 91405, Orsay, France 1085
- 31 ESAC/ESA, Camino Bajo del Castillo, s/n., Urb. Villafranca del Castillo, 28692 Villanueva de la Cañada, Madrid, Spain
- 32 School of Mathematics and Physics, University of Surrey, Guildford, Surrey, GU2 7XH, UK 1090
- 33 INAF-Osservatorio Astronomico di Brera, Via Brera 28, 20122 Milano, Italy
- 34 Université Paris-Saclay, Université Paris Cité, CEA, CNRS, AIM, 91191, Gif-sur-Yvette, France
- 35 IFPU, Institute for Fundamental Physics of the Universe, via Beirut 2, 34151 Trieste, Italy 1095
- 36 INAF-Osservatorio Astronomico di Trieste, Via G. B. Tiepolo 11, 34143 Trieste, Italy
- 37 INFN, Sezione di Trieste, Via Valerio 2, 34127 Trieste TS, Italy
- 38 SISSA, International School for Advanced Studies, Via Bonomea 265, 34136 Trieste TS, Italy 1100
- 39 Dipartimento di Fisica e Astronomia, Università di Bologna, Via Gobetti 93/2, 40129 Bologna, Italy
- 40 INFN-Sezione di Bologna, Viale Berti Pichat 6/2, 40127 Bologna, Italy 1105
- 41 Centre National d'Etudes Spatiales – Centre spatial de Toulouse, 18 avenue Edouard Belin, 31401 Toulouse Cedex 9, France
- 42 Universitäts-Sternwarte München, Fakultät für Physik, Ludwig-Maximilians-Universität München, Scheinerstrasse 1, 81679 München, Germany 1110
- 43 Space Science Data Center, Italian Space Agency, via del Politecnico snc, 00133 Roma, Italy
- 44 Dipartimento di Fisica, Università di Genova, Via Dodecaneso 33, 16146, Genova, Italy
- 45 INFN-Sezione di Genova, Via Dodecaneso 33, 16146, Genova, Italy 1115
- 46 Department of Physics "E. Pancini", University Federico II, Via Cinthia 6, 80126, Napoli, Italy
- 47 Instituto de Astrofísica e Ciências do Espaço, Universidade do Porto, CAUP, Rua das Estrelas, PT4150-762 Porto, Portugal 1120
- 48 Faculdade de Ciências da Universidade do Porto, Rua do Campo de Alegre, 4150-007 Porto, Portugal
- 
- 1 INAF-Osservatorio Astronomico di Padova, Via dell'Osservatorio 5, 35122 Padova, Italy
- 2 Dipartimento di Fisica e Astronomia "G. Galilei", Università di Padova, Via Marzolo 8, 35131 Padova, Italy
- 3 School of Physics, HH Wills Physics Laboratory, University of Bristol, Tyndall Avenue, Bristol, BS8 1TL, UK
- 1030 4 Department of Mathematics and Physics, Roma Tre University, Via della Vasca Navale 84, 00146 Rome, Italy
- 5 INAF-Osservatorio Astronomico di Roma, Via Frascati 33, 00078 Monteporzio Catone, Italy
- 1035 6 Max-Planck-Institut für Astronomie, Königstuhl 17, 69117 Heidelberg, Germany
- 7 INAF-Osservatorio Astrofisico di Arcetri, Largo E. Fermi 5, 50125, Firenze, Italy
- 8 INAF-Osservatorio Astronomico di Capodimonte, Via Moiariello 16, 80131 Napoli, Italy
- 1040 9 School of Physics & Astronomy, University of Southampton, Highfield Campus, Southampton SO17 1BJ, UK
- 10 Jeremiah Horrocks Institute, University of Central Lancashire, Preston, PR1 2HE, UK
- 1045 11 Dipartimento di Fisica e Astronomia "G. Galilei", Università di Padova, Vicolo dell'Osservatorio 3, 35122 Padova, Italy
- 12 INAF, Istituto di Radioastronomia, Via Piero Gobetti 101, 40129 Bologna, Italy
- 13 Institute of Cosmology and Gravitation, University of Portsmouth, Portsmouth PO1 3FX, UK
- 1050 14 Cavendish Laboratory, University of Cambridge, JJ Thomson Avenue, Cambridge, CB3 0HE, UK
- 15 Institute of Space Sciences (ICE, CSIC), Campus UAB, Carrer de Can Magrans, s/n, 08193 Barcelona, Spain

- 49 Dipartimento di Fisica, Università degli Studi di Torino, Via P. Giuria 1, 10125 Torino, Italy
- 1125 50 INFN-Sezione di Torino, Via P. Giuria 1, 10125 Torino, Italy
- 51 INAF-Osservatorio Astrofisico di Torino, Via Osservatorio 20, 10025 Pino Torinese (TO), Italy
- 52 European Space Agency/ESTEC, Keplerlaan 1, 2201 AZ Noordwijk, The Netherlands
- 1130 53 Institute Lorentz, Leiden University, Niels Bohrweg 2, 2333 CA Leiden, The Netherlands
- 54 Leiden Observatory, Leiden University, Einsteinweg 55, 2333 CC Leiden, The Netherlands
- 1135 55 INAF-IASF Milano, Via Alfonso Corti 12, 20133 Milano, Italy
- 56 Centro de Investigaciones Energéticas, Medioambientales y Tecnológicas (CIEMAT), Avenida Complutense 40, 28040 Madrid, Spain
- 57 Port d'Informació Científica, Campus UAB, C. Albareda s/n, 08193 Bellaterra (Barcelona), Spain
- 1140 58 Institute for Theoretical Particle Physics and Cosmology (TTK), RWTH Aachen University, 52056 Aachen, Germany
- 59 INFN section of Naples, Via Cinthia 6, 80126, Napoli, Italy
- 60 Institute for Astronomy, University of Hawaii, 2680 Woodlawn Drive, Honolulu, HI 96822, USA
- 1145 61 Dipartimento di Fisica e Astronomia "Augusto Righi" - Alma Mater Studiorum Università di Bologna, Viale Berti Pichat 6/2, 40127 Bologna, Italy
- 62 Instituto de Astrofísica de Canarias, Vía Láctea, 38205 La Laguna, Tenerife, Spain
- 1150 63 Institute for Astronomy, University of Edinburgh, Royal Observatory, Blackford Hill, Edinburgh EH9 3HJ, UK
- 64 Jodrell Bank Centre for Astrophysics, Department of Physics and Astronomy, University of Manchester, Oxford Road, Manchester M13 9PL, UK
- 1155 65 European Space Agency/ESRIN, Largo Galileo Galilei 1, 00044 Frascati, Roma, Italy
- 66 Université Claude Bernard Lyon 1, CNRS/IN2P3, IP2I Lyon, UMR 5822, Villeurbanne, F-69100, France
- 1160 67 Institut de Ciències del Cosmos (ICCUB), Universitat de Barcelona (IEEC-UB), Martí i Franquès 1, 08028 Barcelona, Spain
- 68 Institució Catalana de Recerca i Estudis Avançats (ICREA), Passeig de Lluís Companys 23, 08010 Barcelona, Spain
- 69 UCB Lyon 1, CNRS/IN2P3, IUF, IP2I Lyon, 4 rue Enrico Fermi, 69622 Villeurbanne, France
- 1165 70 Mullard Space Science Laboratory, University College London, Holmbury St Mary, Dorking, Surrey RH5 6NT, UK
- 71 Departamento de Física, Faculdade de Ciências, Universidade de Lisboa, Edifício C8, Campo Grande, PT1749-016 Lisboa, Portugal
- 1170 72 Instituto de Astrofísica e Ciências do Espaço, Faculdade de Ciências, Universidade de Lisboa, Campo Grande, 1749-016 Lisboa, Portugal
- 73 INFN-Padova, Via Marzolo 8, 35131 Padova, Italy
- 74 Aix-Marseille Université, CNRS/IN2P3, CPPM, Marseille, France
- 1175 75 INFN-Bologna, Via Irnerio 46, 40126 Bologna, Italy
- 76 FRACTAL S.L.N.E., calle Tulipán 2, Portal 13 1A, 28231, Las Rozas de Madrid, Spain
- 77 NRC Herzberg, 5071 West Saanich Rd, Victoria, BC V9E 2E7, Canada
- 1180 78 Institute of Theoretical Astrophysics, University of Oslo, P.O. Box 1029 Blindern, 0315 Oslo, Norway
- 79 Jet Propulsion Laboratory, California Institute of Technology, 4800 Oak Grove Drive, Pasadena, CA, 91109, USA
- 80 Department of Physics, Lancaster University, Lancaster, LA1 4YB, UK
- 1185 81 Felix Hormuth Engineering, Goethestr. 17, 69181 Leimen, Germany
- 82 Technical University of Denmark, Elektrovej 327, 2800 Kgs. Lyngby, Denmark
- 83 Cosmic Dawn Center (DAWN), Denmark
- 1190 84 Institut d'Astrophysique de Paris, UMR 7095, CNRS, and Sorbonne Université, 98 bis boulevard Arago, 75014 Paris, France
- 85 NASA Goddard Space Flight Center, Greenbelt, MD 20771, USA
- 86 Department of Physics and Helsinki Institute of Physics, Gustaf Hällströmin katu 2, 00014 University of Helsinki, Finland
- 87 Université de Genève, Département de Physique Théorique and Centre for Astroparticle Physics, 24 quai Ernest-Ansermet, CH-1211 Genève 4, Switzerland
- 1195 88 Department of Physics, P.O. Box 64, 00014 University of Helsinki, Finland
- 89 Helsinki Institute of Physics, Gustaf Hällströmin katu 2, University of Helsinki, Helsinki, Finland
- 1200 90 Centre de Calcul de l'IN2P3/CNRS, 21 avenue Pierre de Coubertin 69627 Villeurbanne Cedex, France
- 91 Laboratoire d'étude de l'Univers et des phénomènes eXtremes, Observatoire de Paris, Université PSL, Sorbonne Université, CNRS, 1205 92190 Meudon, France
- 92 Aix-Marseille Université, CNRS, CNES, LAM, Marseille, France
- 93 SKA Observatory, Jodrell Bank, Lower Withington, Macclesfield, Cheshire SK11 9FT, UK
- 1210 94 Dipartimento di Fisica "Aldo Pontremoli", Università degli Studi di Milano, Via Celoria 16, 20133 Milano, Italy
- 95 INFN-Sezione di Milano, Via Celoria 16, 20133 Milano, Italy
- 96 University of Applied Sciences and Arts of Northwestern Switzerland, School of Computer Science, 5210 Windisch, Switzerland
- 1215 97 Universität Bonn, Argelander-Institut für Astronomie, Auf dem Hügel 71, 53121 Bonn, Germany
- 98 INFN-Sezione di Roma, Piazzale Aldo Moro, 2 - c/o Dipartimento di Fisica, Edificio G. Marconi, 00185 Roma, Italy
- 99 Department of Physics, Institute for Computational Cosmology, Durham University, South Road, Durham, DH1 3LE, UK
- 1220 100 Université Côte d'Azur, Observatoire de la Côte d'Azur, CNRS, Laboratoire Lagrange, Bd de l'Observatoire, CS 34229, 06304 Nice cedex 4, France
- 101 Université Paris Cité, CNRS, Astroparticule et Cosmologie, 75013 Paris, France
- 1225 102 CNRS-UCB International Research Laboratory, Centre Pierre Binetruy, IRL2007, CPB-IN2P3, Berkeley, USA
- 103 University of Applied Sciences and Arts of Northwestern Switzerland, School of Engineering, 5210 Windisch, Switzerland
- 1230 104 Institut d'Astrophysique de Paris, 98bis Boulevard Arago, 75014, Paris, France
- 105 Institute of Physics, Laboratory of Astrophysics, Ecole Polytechnique Fédérale de Lausanne (EPFL), Observatoire de Sauverny, 1290 Versoix, Switzerland
- 1235 106 Aurora Technology for European Space Agency (ESA), Camino bajo del Castillo, s/n, Urbanización Villafranca del Castillo, Villanueva de la Cañada, 28692 Madrid, Spain
- 107 Institut de Física d'Altes Energies (IFAE), The Barcelona Institute of Science and Technology, Campus UAB, 08193 Bellaterra (Barcelona), Spain
- 1240 108 School of Mathematics, Statistics and Physics, Newcastle University, Herschel Building, Newcastle-upon-Tyne, NE1 7RU, UK
- 109 DARK, Niels Bohr Institute, University of Copenhagen, Jagtvej 155, 2200 Copenhagen, Denmark
- 1245 110 Waterloo Centre for Astrophysics, University of Waterloo, Waterloo, Ontario N2L 3G1, Canada
- 111 Department of Physics and Astronomy, University of Waterloo, Waterloo, Ontario N2L 3G1, Canada
- 1250 112 Perimeter Institute for Theoretical Physics, Waterloo, Ontario N2L 2Y5, Canada
- 113 Institute of Space Science, Str. Atomistilor, nr. 409 Măgurele, Ilfov, 077125, Romania
- 1255 114 Consejo Superior de Investigaciones Científicas, Calle Serrano 117, 28006 Madrid, Spain
- 115 Universidad de La Laguna, Departamento de Astrofísica, 38206 La Laguna, Tenerife, Spain
- 1260 116 Caltech/IPAC, 1200 E. California Blvd., Pasadena, CA 91125, USA
- 117 Institut für Theoretische Physik, University of Heidelberg, Philosophenweg 16, 69120 Heidelberg, Germany

- 118 Institut de Recherche en Astrophysique et Planétologie (IRAP),  
Université de Toulouse, CNRS, UPS, CNES, 14 Av. Edouard Belin,  
31400 Toulouse, France
- 119 Université St Joseph; Faculty of Sciences, Beirut, Lebanon
- 1265 120 Departamento de Física, FCFM, Universidad de Chile, Blanco En-  
calada 2008, Santiago, Chile
- 121 Universität Innsbruck, Institut für Astro- und Teilchenphysik, Tech-  
nikerstr. 25/8, 6020 Innsbruck, Austria
- 1270 122 Satlantis, University Science Park, Sede Bld 48940, Leioa-Bilbao,  
Spain
- 123 Infrared Processing and Analysis Center, California Institute of  
Technology, Pasadena, CA 91125, USA
- 124 Instituto de Astrofísica e Ciências do Espaço, Faculdade de Ciên-  
cias, Universidade de Lisboa, Tapada da Ajuda, 1349-018 Lisboa,  
Portugal
- 1275 125 Cosmic Dawn Center (DAWN)
- 126 Niels Bohr Institute, University of Copenhagen, Jagtvej 128, 2200  
Copenhagen, Denmark
- 127 Universidad Politécnica de Cartagena, Departamento de Elec-  
trónica y Tecnología de Computadoras, Plaza del Hospital 1, 30202  
Cartagena, Spain
- 1280 128 Dipartimento di Fisica e Scienze della Terra, Università degli Studi  
di Ferrara, Via Giuseppe Saragat 1, 44122 Ferrara, Italy
- 129 Istituto Nazionale di Fisica Nucleare, Sezione di Ferrara, Via  
Giuseppe Saragat 1, 44122 Ferrara, Italy
- 1285 130 Department of Physics, Oxford University, Keble Road, Oxford  
OX1 3RH, UK
- 131 Université PSL, Observatoire de Paris, Sorbonne Université,  
CNRS, LERMA, 75014, Paris, France
- 1290 132 Université Paris-Cité, 5 Rue Thomas Mann, 75013, Paris, France
- 133 Zentrum für Astronomie, Universität Heidelberg, Philosophenweg  
12, 69120 Heidelberg, Germany
- 134 INAF-Osservatorio Astronomico di Brera, Via Brera 28, 20122  
Milano, Italy, and INFN-Sezione di Genova, Via Dodecaneso 33,  
16146, Genova, Italy
- 1295 135 ICL, Junia, Université Catholique de Lille, LITL, 59000 Lille,  
France
- 136 ICSC - Centro Nazionale di Ricerca in High Performance Comput-  
ing, Big Data e Quantum Computing, Via Magnanelli 2, Bologna,  
Italy
- 1300 137 Instituto de Física Teórica UAM-CSIC, Campus de Cantoblanco,  
28049 Madrid, Spain
- 138 CERCA/ISO, Department of Physics, Case Western Reserve Uni-  
versity, 10900 Euclid Avenue, Cleveland, OH 44106, USA
- 1305 139 Technical University of Munich, TUM School of Natural Sciences,  
Physics Department, James-Franck-Str. 1, 85748 Garching, Ger-  
many
- 140 Max-Planck-Institut für Astrophysik, Karl-Schwarzschild-Str. 1,  
85748 Garching, Germany
- 1310 141 Laboratoire Univers et Théorie, Observatoire de Paris, Université  
PSL, Université Paris Cité, CNRS, 92190 Meudon, France
- 142 Departamento de Física Fundamental, Universidad de Salamanca,  
Plaza de la Merced s/n. 37008 Salamanca, Spain
- 143 Université de Strasbourg, CNRS, Observatoire astronomique de  
Strasbourg, UMR 7550, 67000 Strasbourg, France
- 1315 144 Center for Data-Driven Discovery, Kavli IPMU (WPI), UTIAS,  
The University of Tokyo, Kashiwa, Chiba 277-8583, Japan
- 145 California Institute of Technology, 1200 E California Blvd,  
Pasadena, CA 91125, USA
- 1320 146 Department of Physics & Astronomy, University of California  
Irvine, Irvine CA 92697, USA
- 147 Department of Mathematics and Physics E. De Giorgi, University  
of Salento, Via per Arnesano, CP-193, 73100, Lecce, Italy
- 148 INFN, Sezione di Lecce, Via per Arnesano, CP-193, 73100, Lecce,  
Italy
- 1325 149 INAF-Sezione di Lecce, c/o Dipartimento Matematica e Fisica, Via  
per Arnesano, 73100, Lecce, Italy
- 150 Departamento Física Aplicada, Universidad Politécnica de Carta-  
gena, Campus Muralla del Mar, 30202 Cartagena, Murcia, Spain
- 151 Instituto de Física de Cantabria, Edificio Juan Jordá, Avenida de los  
Castros, 39005 Santander, Spain
- 152 CEA Saclay, DFR/IRFU, Service d'Astrophysique, Bat. 709,  
91191 Gif-sur-Yvette, France
- 153 Department of Computer Science, Aalto University, PO Box  
15400, Espoo, FI-00 076, Finland 1335
- 154 Instituto de Astrofísica de Canarias, c/ Via Lactea s/n, La Laguna  
38200, Spain. Departamento de Astrofísica de la Universidad de La  
Laguna, Avda. Francisco Sanchez, La Laguna, 38200, Spain
- 155 Ruhr University Bochum, Faculty of Physics and Astronomy, As-  
tronomical Institute (AIRUB), German Centre for Cosmological  
Lensing (GCCL), 44780 Bochum, Germany 1340
- 156 Department of Physics and Astronomy, Vesilinnantie 5, 20014 Uni-  
versity of Turku, Finland
- 157 Serco for European Space Agency (ESA), Camino bajo del  
Castillo, s/n, Urbanizacion Villafranca del Castillo, Villanueva de  
la Cañada, 28692 Madrid, Spain 1345
- 158 ARC Centre of Excellence for Dark Matter Particle Physics, Mel-  
bourne, Australia
- 159 Centre for Astrophysics & Supercomputing, Swinburne University  
of Technology, Hawthorn, Victoria 3122, Australia 1350
- 160 Department of Physics and Astronomy, University of the Western  
Cape, Bellville, Cape Town, 7535, South Africa
- 161 DAMTP, Centre for Mathematical Sciences, Wilberforce Road,  
Cambridge CB3 0WA, UK
- 162 Kavli Institute for Cosmology Cambridge, Madingley Road, Cam-  
bridge, CB3 0HA, UK 1355
- 163 Department of Astrophysics, University of Zurich, Winterthur-  
erstrasse 190, 8057 Zurich, Switzerland
- 164 Department of Physics, Centre for Extragalactic Astronomy,  
Durham University, South Road, Durham, DH1 3LE, UK 1360
- 165 IRFU, CEA, Université Paris-Saclay 91191 Gif-sur-Yvette Cedex,  
France
- 166 Oskar Klein Centre for Cosmoparticle Physics, Department of  
Physics, Stockholm University, Stockholm, SE-106 91, Sweden
- 167 Astrophysics Group, Blackett Laboratory, Imperial College Lon-  
don, London SW7 2AZ, UK 1365
- 168 Univ. Grenoble Alpes, CNRS, Grenoble INP, LPSC-IN2P3, 53, Av-  
enue des Martyrs, 38000, Grenoble, France
- 169 Dipartimento di Fisica, Sapienza Università di Roma, Piazzale  
Aldo Moro 2, 00185 Roma, Italy 1370
- 170 Centro de Astrofísica da Universidade do Porto, Rua das Estrelas,  
4150-762 Porto, Portugal
- 171 HE Space for European Space Agency (ESA), Camino bajo del  
Castillo, s/n, Urbanizacion Villafranca del Castillo, Villanueva de  
la Cañada, 28692 Madrid, Spain 1375
- 172 Dipartimento di Fisica - Sezione di Astronomia, Università di Tri-  
este, Via Tiepolo 11, 34131 Trieste, Italy
- 173 Department of Astrophysical Sciences, Peyton Hall, Princeton Uni-  
versity, Princeton, NJ 08544, USA
- 174 Theoretical astrophysics, Department of Physics and Astronomy,  
Uppsala University, Box 515, 751 20 Uppsala, Sweden 1380
- 175 Minnesota Institute for Astrophysics, University of Minnesota, 116  
Church St SE, Minneapolis, MN 55455, USA
- 176 Mathematical Institute, University of Leiden, Einsteinweg 55, 2333  
CA Leiden, The Netherlands 1385
- 177 ASTRON, the Netherlands Institute for Radio Astronomy, Postbus  
2, 7990 AA, Dwingeloo, The Netherlands
- 178 Center for Advanced Interdisciplinary Research, Ss. Cyril and  
Methodius University in Skopje, Macedonia
- 179 Institute of Astronomy, University of Cambridge, Madingley Road,  
Cambridge CB3 0HA, UK 1390
- 180 Space physics and astronomy research unit, University of Oulu,  
Pentti Kaiteran katu 1, FI-90014 Oulu, Finland
- 181 Center for Computational Astrophysics, Flatiron Institute, 162 5th  
Avenue, 10010, New York, NY, USA 1395
- 182 Department of Astronomy, University of Massachusetts, Amherst,  
MA 01003, USA
- 183 Department of Physics and Astronomy, University of British  
Columbia, Vancouver, BC V6T 1Z1, Canada

1400 **Appendix A: IRAC photometry comparison**

In this Section we show the comparison between the IRAC photometry derived in this work (see Sect. 2.2) and the one from the Cosmic Dawn Survey Catalogue (Euclid Collaboration: Zalesky et al. 2025). This comparison is possible only in the EDF-N and EDF-F, as the Cosmic Dawn Catalogues are not available for the EDF-S. Sources are matched considering a  $1''$  radius, but we verify that the difference does not change significantly considering a smaller matching radius.

As visible in Fig. A.1, the magnitude estimated in our work are, on average, slightly underestimated by  $-0.10$  magnitudes in the EDF-F and  $-0.30$  magnitudes in the EDF-N. These differences are mainly dominated by faint sources as they decrease to  $\Delta\text{IRAC1} = 0.07 \pm 0.34$  and  $\Delta\text{IRAC2} = 0.07 \pm 0.35$  in the EDF-F and  $\Delta\text{IRAC1} = 0.01 \pm 0.34$  and  $\Delta\text{IRAC2} = 0.01 \pm 0.35$  in the EDF-N when we limit the analysis to sources brighter than 21 in the respective bands.

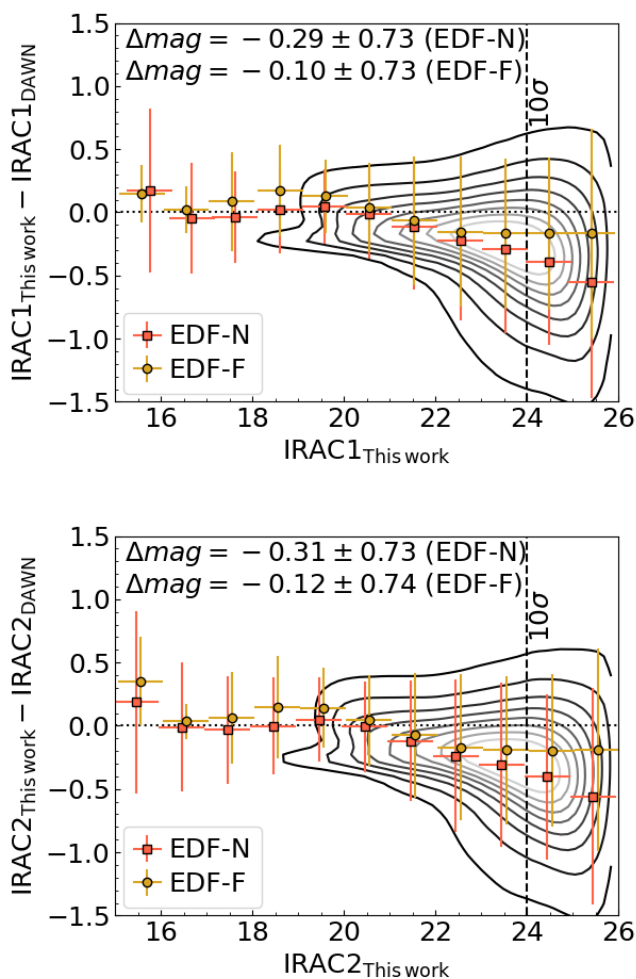


**Fig. A.1.** Difference between the magnitudes derived in this work and the ones in the Cosmic Dawn Catalogue. The black contours show the distribution of all sources in common between the two catalogues (from 10% to 90% of the sample), and red squares and yellow circles show the average values in magnitude bins for the EDF-N and EDF-F, respectively. We report in the top left the mean and standard deviation of the difference in magnitude in the two fields. We report results for the IRAC1 filter on the top and the IRAC2 filter on the bottom panel.

1400 **Appendix B: Redshift recovery**

The *Euclid* pipeline, at the moment, lacks LRD templates. This can have a direct impact on the redshift estimation for these objects. We therefore decided to test the redshift recovery for LRDs by simulating *Euclid* observations of LRDs and input this mock photometry to the *Euclid* pipeline.

In particular, we start by simulating simple LRD spectra, using two power laws, with red and blue continuum slopes at rest-frame optical and UV wavelengths. For the  $\beta_{\text{UV}}$  and  $\beta_{\text{opt}}$  continuum slopes, we considered the values measured by Kocevski et al. (2024) for a sample of 341 LRDs at  $z = 2-11$ , but with a median redshift of  $z = 6.4$ . We used these mock LRDs as templates, moving them from  $z = 1$  to  $z = 7.6$ , where we have enough bands to measure the two slopes in all EDFs. We scale their absolute UV magnitudes ( $M_{\text{UV}}$ ) and compare these with the *Euclid* observational depths. We then derive photometric redshift, considering the same setup used in the *Euclid* pipeline.

In the top panel of Fig. B.1 we report the comparison between the recovered and input redshifts. As can be seen, the first effect is a bimodal distribution, with some galaxies that are wrongly placed at  $z < 2$ . In addition, the output redshift tends to be overestimated for galaxies at  $z_{\text{input}} < 2$ , and the upper limit at  $z = 6$  naturally underestimate the redshift of  $z > 6$  sources. Overall, we have about 40% of outliers ( $f_{\text{out}}$ ), defined as galaxies with  $|\delta z| = |z_{\text{output}} - z_{\text{input}}| / (1 + z_{\text{input}}) > 0.15$ . If we remove these outliers, we obtain a distribution consistent with no redshift bias, since  $\delta z = 0.02 \pm 0.07$ .

In the bottom panel of Fig. B.1 we instead show the comparison between the true redshift and the one recovered by fitting the mock photometry with a double power law and leaving the redshift free to vary (see Sect. 3). In this fit, we considered the pipeline redshift as a starting point and the uncertainties as limits. We verified that leaving the redshift totally free improves the results. This refinement in the redshift produces a substantial reduction in the outlier fraction, more than halving it ( $f_{\text{out}} = 12\%$ ). At the same time, the biases at the different redshifts are similar and the  $z = 6$  upper limit is removed. The expected mean redshift bias, after removing the outliers, is also slightly improved, becoming  $\delta z = 0.01 \pm 0.05$ .

By comparing the intrinsic redshift distribution and the one derived after the two power-law fit, we derived an average redshift correction to apply to the estimated luminosity function (Sect. 4.3). These redshift corrections are derived in redshift bins and are: 0.60 at  $z = 1.0-1.5$ ; 0.91 at  $z = 1.5-2.0$ ; 1.32 at  $z = 2.0-2.5$ ; 1.09 at  $z = 2.5-4.0$ ; and 1.09 at  $z = 4.0-6.0$ .

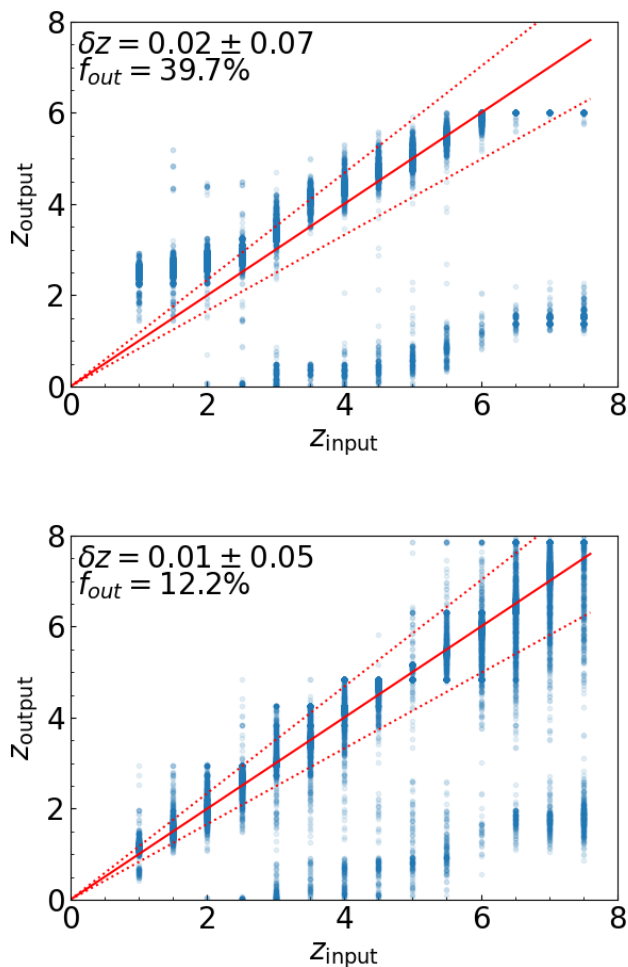


**Fig. B.1.** Redshift recovery using the *Euclid* pipeline (top) and with the double power-law fit improvement (bottom). In the upper right of each panel we report the fraction of outliers, defined as objects with  $|\delta z| = |z_{\text{output}} - z_{\text{input}}| / (1 + z_{\text{input}}) > 0.15$ , the mean and standard deviation of  $\delta z$ , measured after removing the outliers.

## Appendix C: Impact of slope uncertainties on sample selection

In this Section we focus on the impact of the uncertainties of the rest-frame UV and optical slopes on the sample selection. In particular, we start from the subsamples of sources with  $S/N > 3$  in more than four filters. We then randomise the rest-frame UV and optical slopes 100 times, using a normal distribution centred on the best value and with standard deviation equal to the respective uncertainties. After this randomisation, we select for each iteration the number of v-shape sources, checking then the subsample of these objects that is also compact, is not contaminated by nebular emission lines and has a  $\chi^2 < 100$ . We do not perform the visual check of all sources selected in the different iterations.

In [Table C.1](#) we report the 16% and 84% of the distribution of the number of selected objects in the different fields. As visible, the values are larger than the one reported in [Table 3](#), indicating that the number of LRD candidates may be underestimated due to the uncertainties on the rest-frame UV and optical slopes. Because the number of potential contaminants is expected to be

**Table C.1.** 16% and 84% percentages of the number of selected objects when randomising the slope measurements.

	EDF-F	EDF-N IRAC	EDF-S
v-shape continuum	(3700, 3824)	(1997, 2071)	(12 625, 12 839)
Compact	(228, 253)	(100, 120)	(670, 716)
No emission lines	(163, 190)	(49, 62)	(378, 414)
$\chi^2 < 100$	(151, 170)	(38, 49)	(357, 391)
	No-IRAC, $z \leq 2.1$		
v-shape continuum	(112 290, 112 823)	(106 490, 106 997)	(226 002, 226 804)
Compact	(3439, 3533)	(3092, 3189)	(7010, 7144)
No emission lines	(2845, 2936)	(2375, 2451)	(5764, 5890)
$\chi^2 < 100$	(2806, 2900)	(2211, 2287)	(5674, 5798)

larger than the number of LRD, however, we prefer to keep the conservative estimates derived in the main text of this work.

## Appendix D: Complete sample

In [Table D.1](#) we include the final list of LRD candidates and 1485 their properties, derived using the double power law fit described in [Sect. 3](#) and whose performance is shown with mock data in [Appendix B](#).

**Table D.1.** Properties of LRD candidates.

ID	RA [deg]	Dec [deg]	$z$	$\sigma_z$	$M_{UV}$	$\sigma_{M_{UV}}$	$\beta_{UV}$	$\sigma_{\beta_{UV}}$	$\beta_{opt}$	$\sigma_{\beta_{opt}}$
-508115529279019500	50.811552	-27.901950	1.73	0.04	-19.3	0.4	-2.5	0.8	1.3	0.7
-509746984272137369	50.974698	-27.213736	1.43	0.01	-19.1	0.4	-2.3	0.6	0.4	0.4
-506780226277952382	50.678022	-27.795238	1.84	0.09	-19.2	0.2	-2.0	0.5	1.0	0.5
-508524594269841903	50.852459	-26.984190	2.08	0.05	-19.4	0.2	-1.2	0.5	0.2	0.7
-508984186271393227	50.898418	-27.139322	2.04	0.01	-19.1	0.4	-1.3	0.7	0.8	0.9
-509604641270953419	50.960464	-27.095341	1.56	0.07	-18.5	0.5	-1.7	0.8	0.8	0.5
-508222098269760365	50.822209	-26.976036	1.93	0.02	-19.6	0.2	-1.5	0.4	0.2	0.5
-508762123270516640	50.876212	-27.051664	1.56	0.01	-19.4	0.3	-2.6	0.6	0.1	0.5
-508397504271496709	50.839750	-27.149670	2.04	0.07	-19.1	0.4	-1.8	0.9	1.4	1.2
-509723625268249072	50.972362	-26.824907	1.67	0.19	-18.4	0.5	-1.3	0.6	0.4	0.6

**Notes.** Here we report the first 10 objects, and the complete list is available at the CDS.

## Appendix E: Observed properties of the LRD candidates

In Fig. E.1 we report the photometric redshift distribution for the three fields. The average redshift is similar among the three fields and is  $z = 1.7$ . The average redshift of IRAC-detected LRD candidates is larger, that is  $z = 2.4$ , with no LRD candidates at  $z \geq 4$ .

In Fig. E.2 we report the magnitude distributions in the four *Euclid* filters, showing that they are similar for all three fields, with the EDF-N having a light excess at bright magnitudes with respect of the other two fields. Indeed, the mean magnitudes in the EDF-F and EDF-S differ by less than 0.1 mag, and the EDF-N shows slightly brighter magnitudes than the other two fields, with a difference below 0.3 magnitudes. The similarities in the magnitude distributions of the three fields reassures us that the selection is reasonably uniform across these fields.

LRD candidates have mean magnitudes of  $I_E = 25.5$ ,  $Y_E = 24.3$ ,  $J_E = 24.0$ , and  $H_E = 23.7$  and hence are relatively faint. Indeed, only 11% and 8% of them have magnitudes brighter than the  $10\sigma$  depth in the  $H_E$  and  $I_E$  filters, respectively, and these fractions decrease to 7% and 3% in the  $J_E$  and  $Y_E$  filters. The sources detected in IRAC have a mean magnitudes of IRAC1 =

22.2 and IRAC2 = 21.5, showing that they are relatively bright in these two filters. In general, the fit is based only on four filters with  $S/N > 3$  for 20% of the sample, and the remaining sources have from five to 10 filters with  $S/N > 3$ .

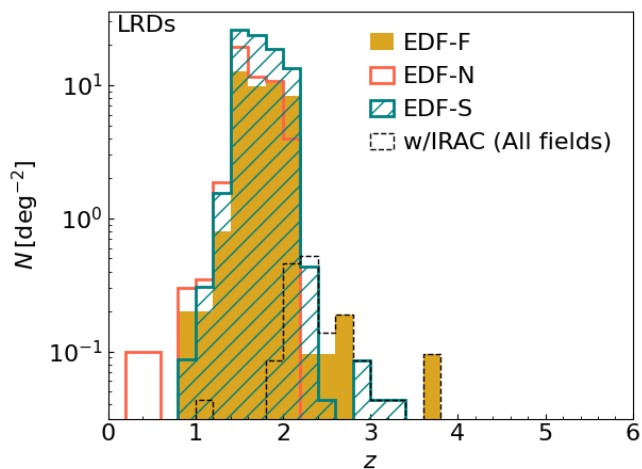


**Fig. E.1.** Photometric redshift distribution of the samples of LRD candidates in the three EDFs. The dotted black histogram shows the overall distribution of sources detected in IRAC.

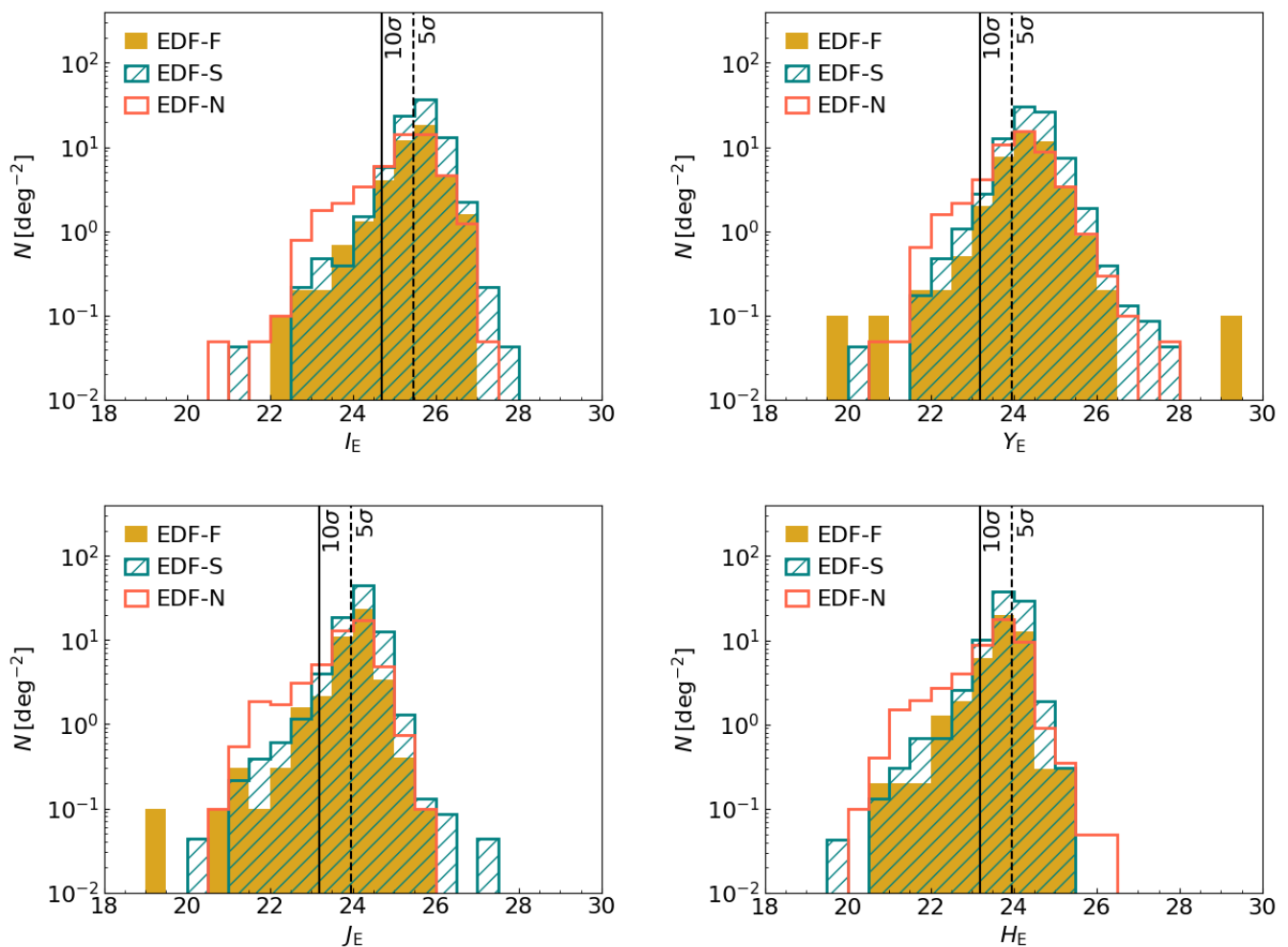


**Fig. E.2.** Magnitude density distribution of the LRD candidates in the three fields in the four *Euclid* filters. The vertical solid and dashed black lines indicate the  $10\sigma$  and  $5\sigma$  depths, respectively.

## Appendix F: Comparison with other *Euclid* AGN catalogues

As mentioned in Sect. 4.2, we verified the overlap between our sample of LRD candidates and other AGN catalogue derived using Q1 data. We give here more information on the criteria used in these other paper, their completeness, purity and level of overlap with our sample.

### Appendix F.1: Optical photometric selections

The first selection presented in [Euclid Collaboration: Matamoro Zatarain et al. \(2025\)](#), named B24A, is based only on two *Euclid* colours and was presented in [Euclid Collaboration: Bisigello et al. \(2024\)](#). Taking into account the limitations of this colour selection, since it has a low purity ( $P = 0.166 \pm 0.015$ ) and a low completeness ( $C = 0.347 \pm 0.004$ ), 254 (8%) of our LRD candidates could be classified as QSO candidates. The selection is indeed based on the  $I_E - J_E$  and  $I_E - Y_E$  colours, so it could trace the blue UV rest-frame slope, which is present in LRDs and blue QSOs, but missing the red optical rest-frame slope.

The presence of observations in the  $u$  band in the EDF-N allows us to use an additional colour selection from [Euclid Collaboration: Bisigello et al. \(2024\)](#), applied again by [Euclid Collaboration: Matamoro Zatarain et al. \(2025\)](#). The selection, which

we refer to as B24B, is based on the  $u - z$  and  $I_E - H_E$  colours, corresponding to a completeness of  $C = 0.861 \pm 0.004$  and a purity  $P = 0.992 \pm 0.017$ . Of the entire sample of LRD candidates in the EDF-N, 258 (26%) are selected by the B24B selection.

In addition, [Euclid Collaboration: Matamoro Zatarain et al. \(2025\)](#) identified two new colour selections fine-tuned based on the colours occupied by DESI QSO. A first selection is based on *Euclid* colours ( $I_E - Y_E$  and  $J_E - H_E$ ) and a compactness criteria, and the second include also ground-based ancillary colours ( $g - z$  and  $I_E - H_E$ ). We refer to this selections as MZ25a and MZ25b, respectively. The first selection includes 1686 QSO candidates, corresponding to 50% of our catalogue, and the second criteria selects 1939 QSO candidates, corresponding to 58% of our catalogue.

The official *Euclid* catalogue ([Euclid Collaboration: Tucci et al. 2025](#)) includes also a probability of being a QSO, obtained by performing a supervised machine learning method called Probabilistic Random Forest (PRF, [Reis et al. 2019](#)), trained using photometric data only. Using this classification, [Euclid Collaboration: Matamoro Zatarain et al. \(2025\)](#) identified QSO as objects having a QSO probability above 85% and not being classified as stars. Of our sample, 34 (1%) LRD candidates are also classified as QSO using this method.

None of our LRD candidates are in the purified subsets of the *Gaia* QSO candidates catalogue (see Sect. 3.2.4. in [Euclid](#)

Collaboration: Matamoro Zatarain et al. 2025) based on the Data Release 3 (DR3, Gaia Collaboration: Vallenari et al. 2023) or in the machine-learning classification based on *Euclid* images by Euclid Collaboration: Margalef-Bentabol et al. (2025).

#### Appendix F.2: Near-IR photometric selections

Taking advantage of the WISE coverage, Euclid Collaboration: Matamoro Zatarain et al. (2025) also applied the two photometric selections by Assef et al. (2018). With the selection corresponding to 75% completeness, called A18C75, 35 (1%) of the LRD galaxies are identified as potential QSOs. With the selection corresponding to 90% reliability, called A18R90, only four LRD candidates are also QSO candidates.

In addition, given that IRAC observations are available for at least part of the sample, we verify if any of our LRD candidates satisfy the AGN selection by Donley et al. (2012). Unfortunately, in the EDF-S this selection can not be applied, as there are observations only on two IRAC bands. In the other two fields, only two LRD candidates has a  $S/N > 3$  in all four IRAC filters and these objects are inside the selection criteria by Donley et al. (2012).

#### Appendix F.3: Spectroscopic selections

The EDF-N is partially covered by DESI EDR (DESI Collaboration et al. 2024), allowing for the classification of QSOs using spectroscopic data. This classification is also included in Euclid Collaboration: Matamoro Zatarain et al. (2025, Sect. 3.3.1) and two LRD candidates (0.2% of our sample in the EDF-N) are indeed classified as QSOs by the DESI spectral type classification and looking at the DESI spectra, having  $FWHM \geq 1200 \text{ km s}^{-1}$  in one of the hydrogen lines. Euclid Collaboration: Matamoro Zatarain et al. (2025) also includes other diagnostic based on spectroscopic DESI spectra, but no LRD candidates are selected by them.

#### Appendix F.4: X-ray AGNs

We now compare our catalogue with the *Euclid* X-ray selected AGN catalogue (Euclid Collaboration: Roster et al. 2025). This catalogue lists the most likely *Euclid* counterparts to the 4XMM DR13, *Chandra* CSC 2.0, and eROSITA DR1 catalogue. While the former two cover the three *Euclid* field in a few, deep pointed observations, the latter covers EDF-F and EDF-S homogeneously but at a shallow depth (see figures 1 and 2 of Euclid Collaboration: Roster et al. 2025).

Out of the entire sample of LRD candidates, three sources (0.09%) are present in the *Euclid* X-ray selected AGN catalogue, two in the EDF-S and one in the EDF-F. The two sources in the EDF-S are matched with sources in the eROSITA DR1, with a probability of being the right counterparts of  $p_{\text{any}} = 0.16$  and 0.97. The source in the EDF-F is matched with a X-ray source in the *Chandra* CSC 2.0 catalogue with a probability of being the right counterparts of  $p_{\text{any}} = 0.98$ . For these sources the chance association can be higher than 80% (see Fig. 7 in Euclid Collaboration: Roster et al. 2025). Out of the three matches, only one has  $S/N > 3$  at (0.5–2.3) keV, that is  $f_{0.5-2.3 \text{ keV}} = (3.92 \pm 1.08) \times 10^{-14} \text{ erg s}^{-1} \text{ cm}^{-2}$ , corresponding to a luminosity of  $2.61 \times 10^{44} \text{ erg s}^{-1}$  at of  $z_{\text{phot}} = 1.1$ . A second source has instead a  $S/N = 2$  at (0.5–2.3) keV, that is  $f_{0.5-2.3 \text{ keV}} = (1.24 \pm 0.62) \times 10^{-14} \text{ erg s}^{-1} \text{ cm}^{-2}$ , and the third

one is below  $S/N < 1$ , with a  $3\sigma$  upper limit of  $f_{0.5-2.3 \text{ keV}} = 5.06 \times 10^{-16} \text{ erg s}^{-1} \text{ cm}^{-2}$ .

Euclid Collaboration: Roster et al. (2025) also identify potential X-ray emitters, using a combination of Bayesian statistics and machine learning. This classification allows us to identify potential X-ray emitters outside the area covered by X-ray observations, which may be useful, for example, for follow up studies. There are 73 LRD candidates that are classified as potential X-ray emitters.

Overall, the small fraction of X-ray LRD candidates of this work is in line with previous works, showing that the majority of LRD are X-ray weak (e.g. Yue et al. 2024), but it is necessary to consider that the X-ray surveys considered here are shallower than the one used to matched previous LRDs selected with JWST. Further analysis of the X-ray emission of these sources in the future could shed light on the AGN contribution in LRDs.

A reassuring result is that all X-ray LRDs have a probability of less than 1% of being Galactic sources. This probability was derived by Euclid Collaboration: Roster et al. (2025) using a random forest algorithm trained on the methodology described in Salvato et al. (2022).